Check for updates

Pushing the limit of 3*d* transition metal-based layered oxides that use both cation and anion redox for energy storage

Minghao Zhang[1], Daniil A. Kitchaev[2], Zachary Lebens-Higgins[3], Julija Vinckeviciute[2], Mateusz Zuba[3], Philip J. Reeves[4], Clare P. Grey[4], M. Stanley Whittingham[3], Louis F. J. Piper[3,5]✉, Anton Van der Ven[2]✉ and Y. Shirley Meng[1]✉

Abstract | Intercalation chemistry has dominated electrochemical energy storage for decades, and storage capacity worldwide has now reached the terawatt-hour level. State-of-the-art intercalation cathodes for Li-ion batteries operate within the limits of transition metal cation electrochemistry, but the discovery of anion-redox processes in recent decades suggests rich opportunities for substantially increasing stored energy densities. The diversity of compounds that exhibit anion redox in the solid state has inspired the exploration of new materials for next-generation cathodes. In this Review, we outline the mechanisms proposed to contribute to anion redox and the accompanying kinetic pathways that can occur in layered transition metal oxides. We discuss the crucial role of structural changes at both the atomic and mesoscopic scales with an emphasis on their impact on electrochemical performance. We emphasize the need for an integrated approach to studying the evolution of both the bulk structure and electrode–electrolyte interphase by combining characterization with computation. Building on the fundamental understanding of electrochemical reaction mechanisms, we discuss engineering strategies such as composition design, surface protection and structural control to achieve stable anion redox for next-generation energy storage devices.

[1]*Department of NanoEngineering, University of California San Diego, La Jolla, CA, USA.*

[2]*Materials Department, University of California Santa Barbara, Santa Barbara, CA, USA.*

[3]*Materials Science & Engineering, Binghamton University, Binghamton, NY, USA.*

[4]*Department of Chemistry, University of Cambridge, Cambridge, UK.*

[5]*Warwick Manufacturing Group, The University of Warwick, Coventry, UK.*

✉*e-mail: Louis.piper@warwick.ac.uk; avdv@ucsb.edu; shmeng@ucsd.edu*

https://doi.org/10.1038/s41578-022-00416-1

Li-ion batteries have dominated battery technologies for portable electronic devices owing to their high specific energy density, thermal stability and long cycle life[1]. The cathode is a critical component of a Li-ion battery because it largely determines the electrochemical performance of the whole system. Starting with the commercialization of $LiCoO_2$-based Li-ion batteries, layered $LiMO_2$ oxides (where M represents a mixture of 3*d* transition metals) have remained the preferred cathode material for commercial Li-ion batteries[2]. The redox process in classical layered oxides is centred on the transition metals, whereby electron extraction from the transition metals is accompanied by some degree of rehybridization between the M *d* orbitals and the O 2*p* orbitals. This redox mechanism explains the capacities that can be achieved upon the near-complete delithiation of layered $LiMO_2$ electrodes[3,4]. Despite annual improvements in the energy density of classical layered oxides, the target energy density of 500 Wh kg^{-1} at the cell level remains elusive, because these materials are limited by both their Li content and the extraction of one electron per transition metal ion.

The limitations of traditional layered $LiMO_2$ cathodes can be overcome in Li-excess $Li_{1+x}M_{1-x}O_2$ systems (Li excess implies that the molar ratio of Li over M is >1 by design), for which the capacity can exceed that expected from transition metal cation redox[5]. The excess capacity has been most frequently attributed to anion-redox processes involving oxygen-dominated states, although other redox processes involving transition metals have also been proposed. Distinct from traditional cation redox, the processes that lead to anomalous capacity in Li-excess materials occur alongside various structural changes that result in degradation, notable voltage hysteresis and long-term voltage fade. The precise relationship between these detrimental features and the redox mechanism remains unknown, leaving open the question of how the promising behaviour of Li-excess systems can be controlled and optimized.

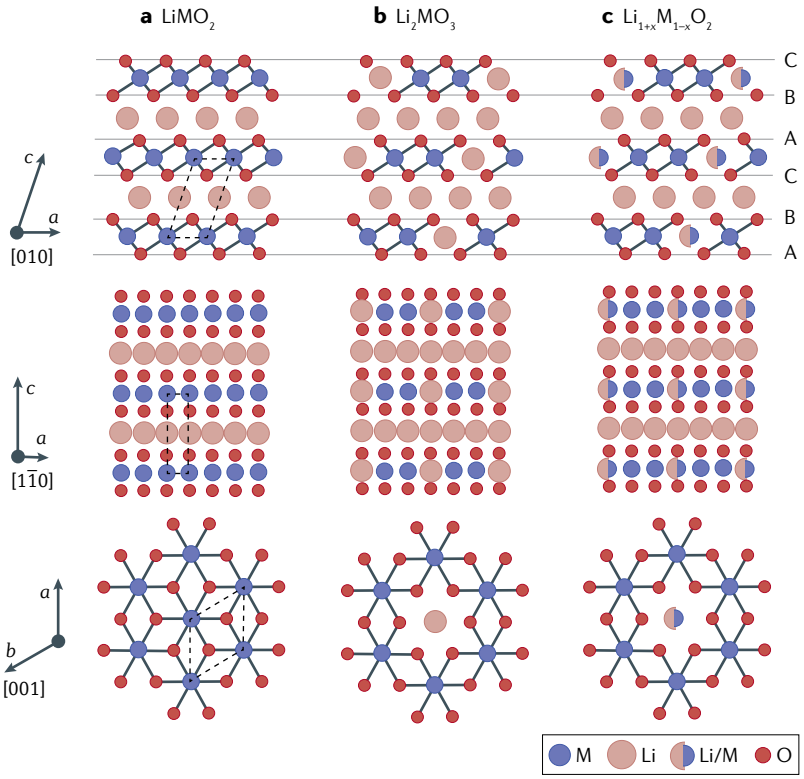

Fig. 1 | **Crystal structures of different types of layered oxides.** Crystal structures of classical layered $LiMO_2$ oxides (panel **a**), Li-excess layered Li_2MO_3 oxides (panel **b**) and Li-excess layered $Li_{1+x}M_{1-x}O_2$ oxides (panel **c**), where M represents 3*d* transition metals. All the structures are based on the primitive cell with the projection axis [010] (top), [1$\bar{1}$0] (middle) or [001] (bottom). The local structure in the transition metal layer for each layered material is magnified on the basis of the [001] projection axis. For simplicity, only the covalent bonding between O and M is shown in each structure. The oxygen stacking sequence perpendicular to the layer direction is shown in the top parts.

Over the past five years, there has been considerable progress towards resolving the mechanisms that underlie anion-redox processes and their relationship to voltage hysteresis and decay. Cathode materials that exhibit anion redox span diverse compositions and crystal structures, including Li-excess layered oxides, Li-excess disordered rocksalts and layered dichalcogenides. Several mechanisms have been proposed to explain the excess capacity of these materials[6–9], including the oxidation of unhybridized O 2*p* orbitals to form localized electron–hole pairs[10,11], O–O dimerization reactions[12] and O_2 gas evolution[13]. Alternatives to pure anion redox have also been proposed, such as transition metal redox beyond the 4+ oxidation state enabled by changes in local coordination[14] and the oxidation of delocalized, π-bonded orbitals formed from hybridized metal and oxygen states (π-redox)[15]. The redox mechanism responsible for the anomalous excess capacity of Li-excess and related cathode materials continues to be debated, and it is likely that multiple mechanisms contribute to the behaviour of different anion-redox systems.

One obstacle to identifying a precise anion-redox mechanism is that the literature on Li-excess materials is vague as to what is meant by anion redox. Although there is a widespread belief that anion redox enables the removal of more Li than is theoretically possible with conventionally understood transition metal redox, there is no consensus on a definition of an anion-redox process. The situation is further confounded by the lack of direct probes capable of distinguishing anion redox from other irreversible reactions that occur in cathode materials, such as decomposition processes and side reactions with (non-optimized) electrolytes. Resolving these uncertainties requires that the charge-transfer processes and structural transformations in Li-excess materials be characterized by a multimodal experimental approach using techniques with the highest possible energy and spatial resolution and in close concert with multiscale computational modelling.

In this Review, we systematize the different reactions that have been proposed for anion-redox materials, including both electrochemical processes and structural transformations. We focus on layered oxide cathodes based on 3*d* transition metals owing to their initial success in Li-ion batteries with carbonate-based electrolytes. We first discuss the crystal structure of these model materials to define the types of bonding environments in which anion redox can occur. We then enumerate and define the possible origins of the excess electronic capacity that have been proposed to explain anion redox and their relationship to the observed electrochemistry. We proceed to summarize the structural transformations that have been documented to accompany anion redox and relate them to the kinetic pathways and crystallographic changes implied by the different redox mechanisms, with an emphasis on defect formation. Finally, we review the experimental and computational probes widely used to study anion redox and conclude by discussing key outstanding questions in the field.

Local coordination of layered oxides

In Li-ion cathode materials, the crystal structure represents an average of local configurations, which has an important role in determining the Li chemical potential and the kinetic mechanisms of Li extraction. The crystal structures of classical $LiMO_2$ layered oxides are based on a close-packed oxygen framework in which the monovalent Li^+ and multivalent M^{n+} ions fill alternating layers of octahedral interstitial sites (FIG. 1a). This structure, referred to as O3, has its oxygen layers stacked in an ABCABC sequence[16]. The 'O' indicates that Li ions are octahedrally coordinated by oxygen, and the '3' indicates that three MO_2 sheets appear in one repeat unit. Following the successful introduction of $LiCoO_2$ in Li-ion batteries, several other layered $LiMO_2$ oxides have been developed through chemical substitution of Co^{3+} with ions such as Ni^{2+}, Ni^{3+}, Mn^{4+} and Al^{3+}. These modifications have increased the practical capacity from 140 mAh g^{-1} to ~200 mAh g^{-1} (REF.[2]).

It is also possible to substitute a fraction of the transition metals M with Li, which results in a class of materials referred to as Li-excess layered oxides[5,17]. The Li ions in the transition metal layers of Li-excess Li_2MnO_3, for example, tend to order in a honeycomb arrangement (FIG. 1b) owing to the large differences in charge and size between Li^+ and Mn^{4+} (REF.[18]). A rich variety of Li-excess layered oxides have been synthesized. Their structure has been described as either a nanocomposite

of layered Li_2MnO_3 and $LiMO_2$ (M = Ni, Co, Mn), or as a single-phase solid solution with the transition metal and Li uniformly mixed while preserving the global honeycomb ordering. The key difference between the two structures is the coherence length of Li_2MnO_3-like domains, which is much shorter in the solid-solution model than in the nanocomposite model. The variation in the coherence length of Li_2MnO_3-like domains in published results may originate from differences in synthesis methods and chemical composition. Independently of the long-range structure used to describe Li-excess materials, NMR has demonstrated the presence of honeycomb-like short-range ordering within the transition metal layers, with Li ions residing at the centre of Mn honeycomb units[18,19] (FIG. 1b,c, bottom). A crucial structural feature of Li-excess materials is that the oxygen ions of the Li_2MnO_3-like ordered domains are coordinated by two transition metals and four Li ions. This coordination is fundamentally different from that of oxygen by three transition metals in classical layered oxides, and creates an unhybridized O *p* orbital, termed an 'orphan orbital' or a 'Li–O–Li' environment[10,11]. A similar orphan orbital can be obtained with vacancies or other coordination chemistries that do not form covalent bonds with oxygen, such as Na–O–Na (REFS[15,20]) or, in theory, other alkali or alkaline-earth elements[21].

Electrochemistry of Li-excess compounds

Voltage curves provide important clues about the electronic and structural changes that occur as an electrode is cycled. The voltage (V) curve of Li-ion batteries with a metallic Li reference anode is linearly related to the Li chemical potential of the cathode ($\mu_{Li}^{cathode}$) according to the Nernst equation: $V = -(\mu_{Li}^{cathode} - \mu_{Li}^{metal})/e$, where e is the charge of an electron and the Li chemical potential of the anode (μ_{Li}^{metal}) is a constant. In turn, the Li chemical potential is derived from the Gibbs free energy of the cathode, and for an intercalation compound is the slope (up to an additive constant that depends on the reference state) of the free energy with respect to Li concentration[22] (FIG. 2). The shape of the voltage profile, therefore, sheds light on the insertion process. For example, Li insertion into a solid solution produces a smooth, sloping voltage curve (FIG. 2a). By contrast, a two-phase reaction manifests as a plateau in the voltage profile, because the chemical potential along the common tangent that bounds a two-phase region is constant with composition (FIG. 2b). The true equilibrium voltage — the open-circuit voltage — is approached only during very slow charging and discharging, and can be measured using galvanostatic or potentiostatic intermittent titration techniques (GITT or PITT, respectively). A charge and discharge cycle at typical rates will result in a voltage profile that is slightly above or below the true equilibrium curve, respectively, owing to sluggish kinetic processes such as diffusion, phase transformations and ohmic losses. This phenomenon leads to polarization relative to the true equilibrium voltage curve (FIG. 2a). It is also possible that the electrode transforms to a new phase at high states of charge and then exhibits a different voltage profile on discharge. This process is illustrated in FIG. 2c, in which the voltage curve on charge (red) is derived from a different free-energy surface than the one followed on discharge (blue). The turquoise arrow at the end of charge signifies a chemical (as opposed to electrochemical) transformation of the charged electrode to a more stable phase (blue free-energy curve). A different discharge voltage profile can also arise from a different reaction pathway owing to the gradual increase in the extent of structure evolution during the charge process.

FIGURE 3a illustrates a schematic voltage profile of a typical Li-excess layered oxide, based on reported experimental data[23]. This voltage profile shows four features that remain to be adequately explained. The first is the activation 'plateau' at ~4.5 V, exhibited by most Li-excess materials that contain Mn, during the first charge. The onset of the activation plateau occurs once all transition metal cations have reached a formal oxidation state of 4+. Although the activation plateau is suggestive of a two-phase reaction, there is no conclusive in situ diffraction data indicating a two-phase co-existence along the activation plateau, as is required, in principle, to label a process as a 'plateau'. A second mystery pertains to the qualitative change in the shape of the voltage profile between the first charge (red curve) and the first discharge (blue curve). Owing to the relationship between a voltage curve and the free energy of the electrode, such a change in shape is strong evidence that the material on discharge is structurally different from that on charge as a result of phase transformations, assuming that the electrochemistry is not dominated by parasitic reactions with the electrolyte or a carbon additive at these potentials. It is now well established that transition metals migrate during the first-charge process to produce a more disordered electrode material[24]. However,

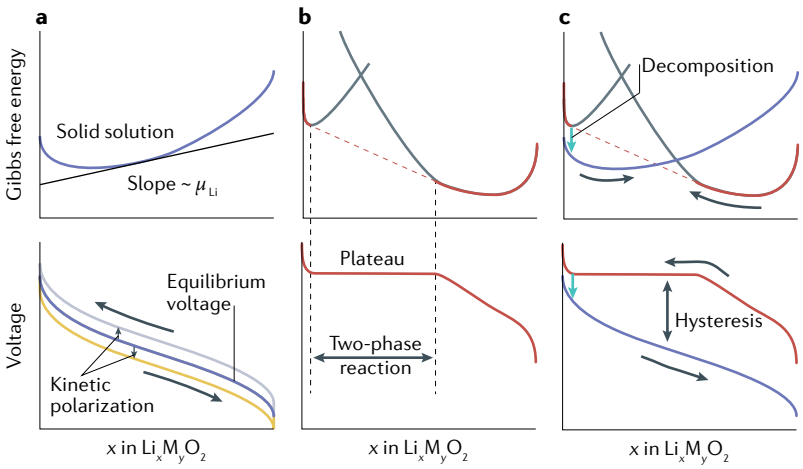

Fig. 2 | **Relationship between voltage curves and Gibbs free energy.** The equilibrium voltage curve of a Li-ion battery is related to the derivative of the Gibbs free energy of the cathode according to the Nernst equation. **a** | A solid solution with a convex free-energy surface exhibits a sloping voltage curve (where μ_{Li} is the Li chemical potential of the electrode and corresponds to the slope of the free energy with respect to Li concentration (x)). Kinetic processes such as diffusion require an overpotential, which leads to polarization in the voltage profile with the charge curve (grey) and discharge curve (yellow) being higher and lower than the true equilibrium curve (blue), respectively. **b** | A two-phase reaction appears as a plateau in the voltage profile. **c** | The voltage curves of the charge (red) and discharge process (blue) may differ if the electrode follows a different path during charge and discharge. In all the Gibbs free-energy diagrams, black curves bound a two-phase region, whereas red or blue curves represent a single-phase region.

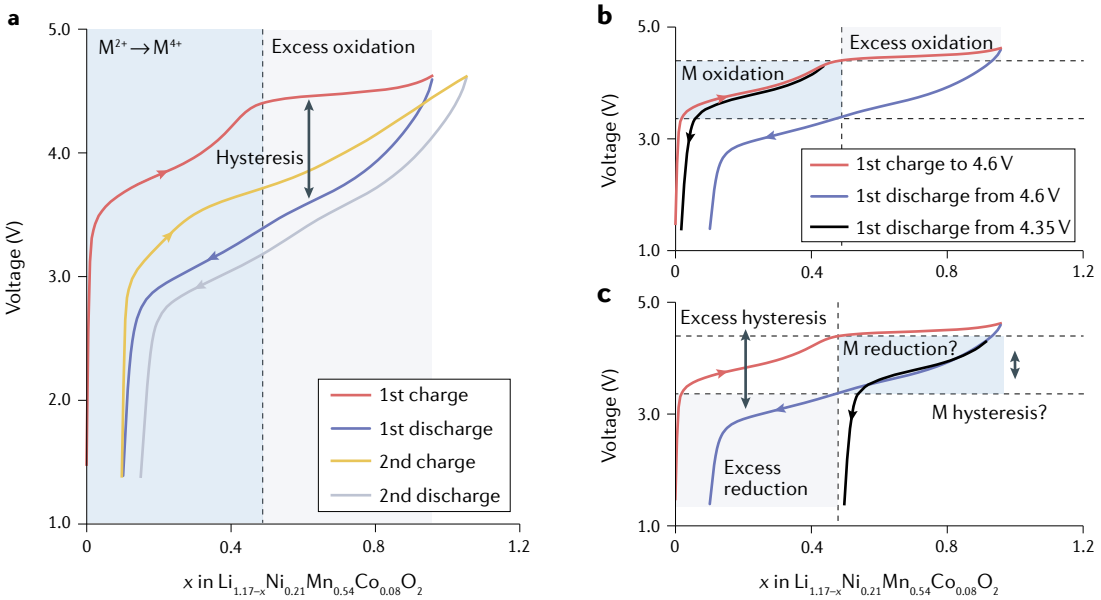

Fig. 3 | **Common features of voltage curves for Li-excess layered oxides. a** | Illustration of the common features displayed by the voltage curve of almost all Li-excess materials that contain Mn, including the activation plateau at ~4.5 V, a change in the shape of the charge and discharge voltage curves, and persistent hysteresis. **b** | The shape of the voltage curve changes upon discharge only after the electrode has been charged through the activation plateau above 4.5 V. **c** | To illustrate one proposed discharge mechanism wherein the order of conventional and anion redox switch between charge and discharge, the discharge curve of the partially charged electrode (black) is shifted so that it overlies the discharge curve of the fully charged electrode (blue) at the beginning of discharge. M, 3*d* transition metal. Adapted from REF.[23], CC BY 4.0.

an unanswered question is whether cation migration is crucial for enabling the redox process during the activation plateau, or whether it is a side effect of this redox process. A third mystery relates to the origin of the persistent hysteresis between subsequent charge and discharge steps. The shapes of subsequent charge curves (yellow) differ slightly from those of the discharge processes (grey), indicating that the electrode follows a different reaction pathway during charge and discharge. A consensus is emerging that transition metal migration has an important role during subsequent cycles and that their sluggish mobility relative to that of Li ions is in part responsible for differences in the reaction pathways between charge and discharge[23,25,26]. A fourth unexplained phenomenon is the origin of the progressive voltage fade exhibited by Li-excess materials during each subsequent cycle. Although the details remain to be established, progressive voltage fade is not especially surprising, given that Li-excess materials in their charged states are highly metastable and that multiple charge and discharge cycles increase the probability that the electrode material is able to find a more stable structure, especially in the charged state.

FIGURE 3b shows that Li-excess electrodes undergo notable changes only after passing through the activation plateau. If discharged before the activation plateau, the voltage curve (black) is qualitatively unaffected. Some reports suggest that even if the material is charged through the activation plateau, the initial discharge is dominated by the same transition metal reduction process as in the partially charged case[23,27,28]. To illustrate this scenario, it is insightful to shift the discharge curve of the partially charged electrode (black curve) to overlap with the discharge curve of the fully charged electrode (blue curve) (FIG. 3c). The shapes of the two voltage curves at the early stages of discharge are very similar, suggesting that conventional transition metal redox may be responsible for the initial capacity recovered on discharge of the fully charged electrode (blue curve). The curves deviate at lower voltages and higher states of discharge, implying that the redox processes responsible for the excess capacity on discharge of the fully charged electrode (blue curve) occurs over a voltage window that is considerably lower than that of the activation plateau of 4.5 V, at which the excess capacity was accessed on charge. The true hysteresis between the redox processes responsible for the excess capacity on charge and those responsible for the excess capacity on discharge may, therefore, be even larger than the apparent hysteresis, as measured by the difference in voltage curves at fixed concentration. FIGURE 3c indicates a voltage hysteresis that is >1 V. Finally, it is worth noting that recent reports of other anion-redox materials designed to partially resist decomposition indicate that the voltage hysteresis, if present, is not universal, with anion reduction preceding transition metal reduction in spectroscopic data[29].

Possible redox mechanisms

There is no known redox mechanism that can explain all of the above electrochemical observations in Li-excess layered materials. Furthermore, it is not unlikely that different redox mechanisms dominate depending on the composition and structure of the Li-excess material. Although it is widely held that the excess capacity has

its origin in an anion-redox process, the literature on Li-excess materials is often vague in its terminology. Precise definitions of distinct redox mechanisms are essential for the correct interpretation of experimental observations and critical evaluation of the multitude of theories that have been put forward to explain the unique electrochemical behaviour of Li-excess materials. Understanding the redox mechanism is necessary to pinpoint the structural degradation process and to systematically resolve performance issues in these materials. We now identify five broad categories of redox processes that have been proposed to occur during the cycling of Li-excess materials.

Coordination-preserving transition metal redox. Coordination-preserving transition metal redox refers to the redox processes of classical layered intercalation compounds, such as Li_xCoO_2, Li_xNiO_2, $Li_x(Ni_{1-y-z}Co_yAl_z)O_2$ (NCA) and $Li_x(Ni_{1-y-z}Mn_yCo_z)O_2$ (NMC) (with $x \leq 1$ in all these compounds), in which transition metals remain in their original crystallographic site as the Li concentration is varied. Transition metal redox in intercalation compounds is frequently accompanied by a notable degree of rehybridization of the M–O bonds, which often results in redistribution of charge between the metal and oxygen[30–32] (FIG. 4a). In some cases, the rehybridization can lead to large changes in the local electron charge around oxygen, with little variation in charge on the transition metal, thereby suggesting an anion-redox process[33]. Spectroscopic signatures used to assign oxygen redox have been reported at the highest states of delithiation in classical layered compounds[34]. Nevertheless, although oxygen may actively participate through rehybridization, the redox process would not occur without a nearby (or coordinated) redox-active transition metal and does not lead to higher capacities than would be expected from a change in the formal oxidation state of the transition metal.

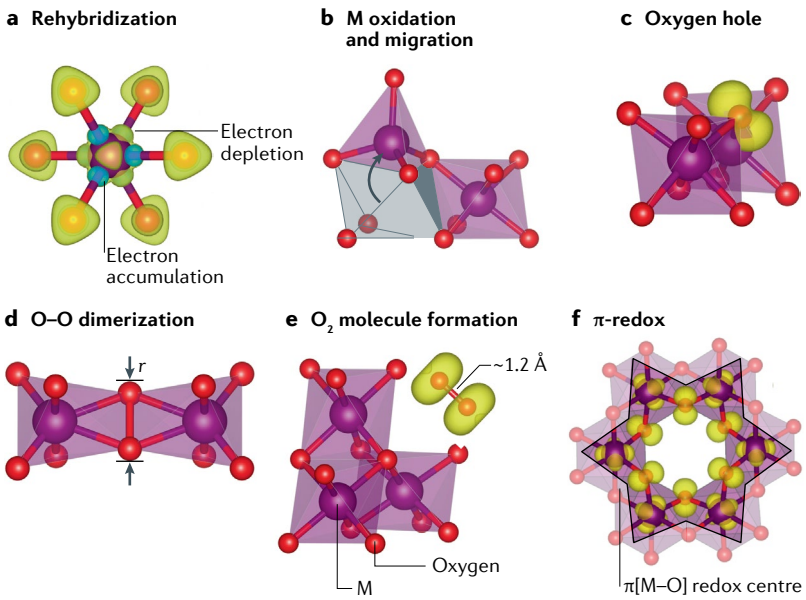

Fig. 4 | **Distinct redox mechanisms for Li-excess layered oxides. a** | Coordination-preserving transition metal redox is usually accompanied by notable rehybridization between the transition metal (M) and its coordinating oxygen ions. Oxygen is in red, M in purple and electron density isosurface contour plots in yellow and light blue. **b** | Some transition metal redox processes require a change in coordination, leading to transition metal migration. **c** | In undercoordinated oxygen ions in Li-excess materials, holes can form in orphan oxygen *p* orbitals. **d** | Anion redox can be accompanied by structural distortions such as O–O dimer formation. The dimer distance (*r*) can be >2 Å or as short as in molecular O_2^{n-} species (~1.2–1.6 Å). **e** | Oxygen dimers can detach from the crystal and either remain trapped in sub-nanometre-sized pockets or migrate to the surface, where they leave the crystal irreversibly. **f** | π-hybridization between non-bonding metal *d* and oxygen *p* orbitals can form a delocalized redox centre.

Coordination-changing transition metal redox. Coordination-changing transition metal redox applies to processes that involve transition metals such as Cr and Mn, among others, that can access oxidation states beyond 4+ but require a change in coordination to achieve these higher oxidation states. For example, whereas Mn^{4+} prefers octahedral coordination, Mn^{7+} prefers tetrahedral coordination. The redox process is thus coupled to transition metal migration (FIG. 4b). Although the electrochemical formation of tetrahedral Mn^{7+} has, to date, been proposed only theoretically[14,27], oxidation-coupled Cr migration has been observed by various experimental and computational techniques[35–38]. In these compounds, the oxidation from Cr^{3+} to Cr^{6+} triggers Cr migration from octahedral sites to tetrahedral sites[39,40]. An important consequence of this oxidation mechanism is that it results in a local structural change that must be retraced with precision during reduction (that is, with the same coupling between migration and the redox process upon Li removal versus insertion) to prevent irreversibility and hysteresis. Such non-hysteretic metal migration is unlikely in most crystal structures and under practical electrochemical testing conditions.

Lattice oxygen redox. The term 'lattice oxygen redox' has been used to refer to redox processes that involve undercoordinated oxygen ions — a local coordination feature of almost all Li-excess compounds — and has been predicted to occur theoretically[10]. Electrons are extracted from non-bonding *p*-like states (FIG. 4c), termed orphan orbitals, which leads to a change in the formal valence of the affected oxygen ion from O^{2-} to O^{n-} (where $n < 2$). The redox mechanism leaves the oxygen ion in place within the crystal, although slight distortions involving shortening of O–O bond lengths between nearest-neighbour oxygen ions have been proposed as a possible consequence of the redox process. This bond shortening includes distortions towards neighbouring oxygen ions that are also oxidized to form what have been termed 'dimers' through a reductive coupling mechanism[21,41] (FIG. 4d). The bond lengths (*r*), however, remain much longer than the short bonds characteristic of the covalent interactions in molecular oxygen or the peroxide and superoxide anions.

Molecular oxygen redox. Molecular oxygen redox also involves oxygen ions but results in distinct structural changes and the formation of stable covalent bonds. In this process, a pair of oxygen ions either forms a dimer with short bond lengths[42,43] (FIG. 4d, $r \approx 1.2–1.6$ Å) or detaches from the crystal to form a molecular species

such as O_2 or O_2^{n-} that occupies a small pocket within the crystal[14,27,44,45] (FIG. 4e). Before the redox process, the oxygen ions have a formal oxidation state of O^{2-}, which changes to O^0 when they combine to form a neutral oxygen molecule or O^{1-} in a peroxide molecule (O_2^{2-}). Other molecular species are also possible, such as O_2^- and O_2^{3-} (REFS[25,46]). A crucial feature of the molecular oxygen redox mechanism is that two oxygen ions form a short, covalent bond in the range 1.2–1.6 Å, which results in notable local changes to the crystal structure either through lattice distortion or cation migration.

Delocalized π-redox. Delocalized π-redox is a recently proposed mechanism that connects traditional transition metal redox with the lattice oxygen redox hypothesis[15]. In this mechanism, non-bonding transition metal *d* orbitals form π bonds with non-bonding O *p* orbitals to create an extended molecular orbital that is redox active (FIG. 4f). Because this redox-active orbital is delocalized between multiple transition metal and oxygen atoms, the process can no longer be described in terms of atomic oxidation states, but rather as a hybridized redox centre over an extended molecular unit. An important consequence of this mechanism is that the oxidation potential, stability and structural evolution are highly dependent on the connectivity of the π-redox centre and, thereby, the long-range structure of the material. Furthermore, the reliance of π-redox on the presence of transition metal electrons implies that this type of oxidation is not possible with d^0 transition metal ions.

It should be emphasized that although there are well understood spectroscopic signatures to identify transition metal redox (both coordination-preserving and coordination-changing) and molecular oxygen redox, the lattice oxygen redox and delocalized π-redox mechanisms have only recently been theorized and their spectroscopic signatures have not yet been definitively established.

Kinetic pathways and structural evolution

It is next instructive to enumerate the different structural transformations that can occur as a Li-excess material is cycled, their kinetics and their relationship to the possible redox mechanisms. The qualitative differences between the first charge and first discharge voltage curves of a Li-excess material strongly suggest that irreversible crystallographic changes of the host begin to occur as early as the activation step on first charge. This interpretation is supported by numerous structural studies that have shown evidence of transition metal migration during the 4.5-V activation 'plateau'[47]. Although all five redox mechanisms discussed above can occur reversibly, three among them (coordination-preserving transition metal redox, lattice oxygen redox and delocalized π-redox) do not require a structural transformation. If these redox mechanisms are responsible for the anomalous capacity of Li-excess materials, then the observed structural changes can be viewed as collateral damage of the redox process. By contrast, coordination-changing transition metal redox and molecular oxygen redox involve structural changes that must be undone if the material is to be restored to its original state during discharge. If these mechanisms are the source of excess capacity, then the irreversible structural changes observed in these materials are an integral part of the redox process and a way must be found to make these structural changes reversible. Unfortunately, the crystallography of current Li-excess materials is such that transition metal migration or the formation of short, covalent O–O bonds opens up a multitude of new pathways during the reverse process, thereby greatly enhancing the probability of irreversibility and hysteresis. Beyond the local crystallographic changes, the structural evolution increasingly assumes dimensions that span the nanoscale and macroscale during each subsequent cycle, as described in this section.

Transition metal migration. The driving forces that trigger transition metal migration during the activation plateau remain to be established. It has been argued that lattice and molecular oxygen redox destabilize M–O bonds and thereby spur transition metal migration to the emptied Li layers[23] (FIG. 5a). This process is often accompanied by an intermediate state with the tetrahedral site occupied by Li or M. In-plane transition metal migration may also occur as the Li ions of the transition metal layers are removed during charge, thereby leaving vacancies[47–49]. In-plane migration does not alter the global layered structure of the compound, but it does disrupt the honeycomb superstructure within the transition metal layers (FIG. 5a). Both out-of-plane and in-plane transition metal migration during the activation plateau result in a new material at the end of the first charge and, hence, a different voltage profile on discharge. In both cases, the assumed redox mechanism implies that transition metal migration is a side effect that occurs after lattice and/or molecular redox have taken place. An alternative mechanism suggests the opposite, wherein Mn migration is key to the redox process[14]. This mechanism relies on coordination-changing transition metal redox, whereby Li extraction is accommodated by Mn redox from 4+ to 7+ coupled with migration from octahedral to tetrahedral coordination. The mechanism implies the presence of high concentrations of Mn^{7+} in tetrahedral sites at the end of charge, for which there is little experimental evidence[14]. However, the migration to tetrahedral sites may be the first step along a decomposition pathway to a lower-energy state that consists of densified oxide and O_2 molecules[14,27]. Subsequent migration of Mn to octahedral sites is possible, but would be accompanied by a reduction from 7+ back to 4+ coupled with the formation of molecular oxygen species to compensate for the reduction of Mn (REF.[27]). In this scenario, the electrochemical redox process of the activation plateau is due to Mn, but a side effect is the evolution of molecular O_2^{n-}-like species that are either trapped in the crystal or coalesce in internal pockets[14].

Oxygen vacancies and internal pockets. Initial studies on Li-excess materials attributed the activation plateau to the equilibrium reaction[50]:

$$Li_2MnO_3(s) \rightarrow MnO_2(s) + 1/2O_2(g) + 2Li^+ + 2e^-$$

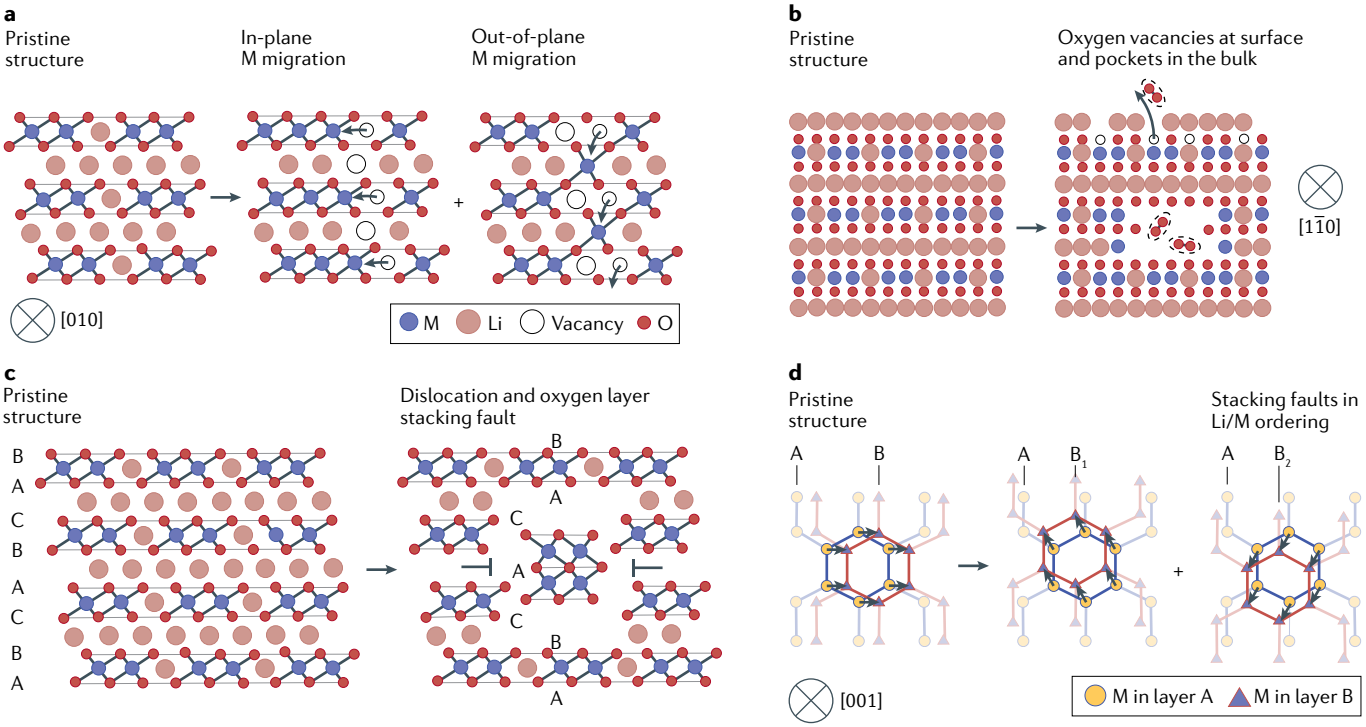

Fig. 5 | **Structural evolution scenarios during or after oxygen-redox activation. a** | Formation of Li vacancies and in-plane and out-of-plane transition metal (M) migration. **b** | Formation of oxygen vacancies on the crystal surface and the internal growth of pockets filled with O_2-type molecular species. **c** | Evolution of the local oxygen stacking sequence induced by the formation of a dislocation network. **d** | Transition metal stacking fault along the [001] projection that breaks down the superlattice ordering. The translation vector between neighbouring transition metal layers (A and B) is [1/3, 1/3, 1/3] for ordinary O3 stacking based on the rhombohedral unit cell (left). Two other possible translations with vectors [2/3, 0, 1/3] and [0, 2/3, 1/3] create two more triangular lattice planes B_1 and B_2 (right), which are considered to be stacking faults of the transition metal layers.

The end state of this reaction has the lowest free energy of all the competing reaction products[27]. However, under realistic conditions, the voltage of this reaction is ≪4.5 V, indicating that the equilibrium reaction cannot be solely responsible for the observed voltage profile, even in phase-pure Li_2MnO_3. The equilibrium reaction leads to irreversible oxygen loss and the densification of the transition metal oxide. Although there is experimental evidence that oxygen evolution does occur, it is restricted to the particle surface and to additional surfaces caused by particle cracking[51]. Furthermore, if oxygen loss were to occur to completion, it would not allow for the excess capacity that is reproducibly observed in subsequent cycles of Li-excess layered materials. A closely related mechanism also involves release of bulk oxygen from the surface according to the above reaction, but skips the transition metal densification process. The resultant reaction product is a highly metastable structure that contains a high concentration of oxygen vacancies while simultaneously preserving the original Li sites within the transition metal layer[49]. This mechanism would require high oxygen mobilities in layered and rocksalt-based intercalation compounds, for which there is currently little evidence. Nevertheless, such a reaction product, with a stoichiometry of MO_2, would contain sufficient Li sites to accommodate the excess Li of the original material upon discharge. The reinsertion of all extracted Li would lead to reduction of a fraction of transition metals to 2+ (as opposed to 3+).

There is little evidence that the equilibrium reaction involving the irreversible evolution of molecular O_2 at the surface is responsible for the anomalous capacity of Li-excess materials during the activation plateau, but recent work has suggested that the reaction might occur locally within the bulk of the crystal, leading to nanoscale pockets of trapped O_2 molecules and a local rearrangement of transition metals[27,44,45] (FIG. 5b). First-principles studies of Li_2MnO_3 have indicated that the localized hole on oxygen created during lattice oxygen redox is unstable with respect to oxygen dimerization in the fully delithiated state, leading to the formation of O_2-type molecular species within the crystal[44]. It has been proposed that the reaction is reversible in the sense that the trapped O_2 molecules can cleave to enable oxygen reattachment to the crystal upon Li reinsertion[45]. Such a process has similarities to oxygen redox in Li_2O/Li_2O_2 conversion[52,53]; in this case, the pure anion redox has enabled a 500 Wh kg^{-1} pouch-type Li-metal cell with ~80% energy density retention after 100 cycles[54]. This mechanism suggests that the above equilibrium reaction does occur, but within the bulk of the crystal and in a way that ensures that oxygen molecules are not irreversibly lost but instead remain available during discharge. The local reorganization of transition metal ions, which leads to rocksalt-like and

spinel-like regions, nevertheless has much in common with the phenomena at the surface when the equilibrium reaction occurs there[55] (FIG. 5b). Future advances in controlling the reversible electrochemical generation of covalent O_2 species may open up routes to decreasing the hysteresis that plagues these reactions and extend beyond the Li-ion chemistries discussed here.

Dislocations and stacking faults. Independently of crystal-structure transformations, Li-excess layered materials undergo pronounced changes in their mesostructure. Upon the first charge, nanoparticles of Li-excess materials nucleate a mobile dislocation network with a dislocation density at least one order of magnitude larger than that of classical layered NCA particles at high states of charge[56]. A key effect of these line defects is to create new local environments for Li ions by perturbing the stacking sequence of oxygen layers (FIG. 5c). First-principles studies indicate that these new environments modify the Li-site energy, which results in a change of the voltage profile on discharge[57]. A secondary effect is that dislocations can serve as short-circuit diffusion channels for oxidized oxygen species, facilitating their transport to the electrode surface where irreversible O_2 loss may occur. The high dislocation density can be explained by two mechanisms relevant to electrode charging. First, the decrease in Li diffusivity during activation, from $10^{-14}\,cm^2\,s^{-1}$ at 4.0 V to $10^{-15}\,cm^2\,s^{-1}$ at 4.4 V (REF.[58]), leads to steep gradients in Li concentration, which may translate into substantial coherency stresses from the variation in the equilibrium lattice parameter. Second, transition metal migration and the possible formation of oxygen vacancies may lead to vacancy loops that are equivalent to edge dislocations that extend across the nanoparticle. This mechanism is consistent with an increase in transition-metal-layer stacking faults (FIG. 5d) after the activation plateau, which can be observed as offsets and streaking in diffraction spots[59]. Although it remains unclear how these planar defects may contribute to voltage hysteresis and further structural degradation, they can, at minimum, accommodate the strain accumulated during cycling. Finally, as with local structural transformations, these mesoscale changes break down the ordering of the pristine electrode and create a metastable structure that is responsible for the evolution of the voltage profile and electrochemical hysteresis. Under moderate heating, these defects can be annealed to recover the original, equilibrium structure, along with the first-cycle electrochemical voltage profile[57].

Consequences of structural evolution. The three categories of structural changes that are triggered upon passage through the activation plateau have important consequences for long-term cycle stability. Transition metal migration, oxygen detachment coupled with the formation of trapped O_2^{n-} species, and the creation of extended defects lead to an increase in both the degree of disorder among the transition metals and in the number of structural defects that can facilitate irreversible kinetic processes during subsequent cycles. The original long-range ordering among the transition metals is never recovered upon Li reinsertion unless the discharged electrode is annealed at high temperature[24,57]. Subsequent cycling causes further disordering among the transition metal cations that is accompanied by irreversible phase transformations. The continued evolution of the structure at multiple length scales brings the original material closer to states that usually consist of densified transition metal oxides and irreversibly released O_2 gas.

Quantitative characterization of anion redox

There is no single characterization technique that can distinguish the multitude of possible processes that underlie anion redox; thus, a multimodal characterization approach is required to make unambiguous statements about this redox mechanism. An extensive range of well established magnetic[4,60,61], structural[62–65] and electronic[23,29,66–72] techniques have been used to capture formal transition metal redox in ex situ[23,65,67] and operando[60,64,70–72] conditions. Properly identifying anion redox candidates requires suitable oxygen-sensitive spectroscopies in tandem with structural probes. Compared with transition metal probes, oxygen-specific techniques are typically more specialized, involving advanced X-ray or neutron facilities, and are not as well suited for operando studies. Experimental techniques of interest for examining anion redox are summarized in TABLE 1. Computational studies based on atomistic simulations are an essential part of the characterization effort and are required to filter out improbable scenarios and to help interpret ambiguous signals.

Addressing the capacity contributions. In the absence of conventional transition metal redox, additional capacity either originates from side reactions or charge-compensation mechanisms that differ from formal transition metal redox. For layered oxide cathodes, the primary side reactions involve Li_2CO_3 breakdown, electrolyte degradation and oxygen loss from the lattice, giving rise to CO, CO_2 and O_2 gas release[11,73–75]. Differential electrochemical mass spectrometry (DEMS) is the technique best suited to distinguishing and quantifying these side-reaction components[73,74]. We note that the possibility of singlet oxygen formation during delithiation of layered oxide cathodes requires isotope labelling to deconvolute the stoichiometry of gas released from the chemical or electrochemical process[76,77]. DEMS has revealed that the excess capacity for the Li_2MnO_3 parent compound is largely accounted for by O_2 loss and CO_2 generation, with minimal contributions from bulk redox processes[51,78,79]. Although Li_2MnO_3 is often viewed as an essential component of the Li-excess NMC material when considering it as a nanocomposite ($xLi_2MnO_3\bullet(1-x)LiMO_2$), Li_2MnO_3 by itself does not display the bulk charge-compensation mechanisms of the Li-excess nanocomposites. Turning to the electrochemistry of classical and Li-excess layered oxides (FIG. 6a,b), gas release is typically observed only towards the end of charge[73,74]. Although gas release tends to be higher for the Li-excess NMC systems, the quantity of gas released is not enough to explain the excess capacity beyond formal transition metal redox and can be greatly suppressed with surface modifications[13,80]. For Li-excess NMC, this result is direct evidence that a large portion

Table 1 | **Experimental techniques for capturing the direct and indirect effects of non-conventional cationic redox**

Technique	Operando or ex situ?	Depth	Notable result	Pros	Cons	Comments	Refs
DEMS	OD	Full system	O_2 gas mass spectrometry	Quantifies gas evolution (originating from the surface); probes electrolyte and cathode side reactions; isotope labelling (^{16}O and ^{18}O)	Possible depth limitation of isotopic elements within the bulk of the sample	Well established for characterizing side reactions	11,51, 73–75,78
Oxygen K-edge sXAS	ES	5 nm (EY); >100 nm (FY); bulk (STXM)	531-eV sXAS peak	Direct sensitivity to O^{n-}	O^{n-} overlaps with M *d*–O 2*p* pre-edge peaks	Non-equilibrium electronic structure calculations needed	23,81–84
Oxygen K-edge RIXS	ES	>100 nm (FY)	RIXS loss peaks assigned to features observed in both Li_2O_2 and O_2 references	Direct probe of oxidized O; relative O^{n-}quantification	Performed ex situ	First-principles spectral simulations needed	11,23,45, 51,65,69, 75–77,80, 84,87–93, 105
XPS, HAXPES	ES	1–5 nm (XPS); 15–25 nm (HAXPES)	O 1s: 530–531 eV peak	Can be used to probe chemical bonding of both M and O	Surface sensitivity	Not a good probe of bulk peroxides but suitable for surface O environments	51,94–97
Acid titration + DEMS	ES	Full system	O_2 gas mass spectrometry	Absolute quantification of bulk oxidized O	Ignores O_2 gas dissolution in the electrolyte; difficult to distinguish O evolution from other oxidized species	Needs benchmarking	74,80
EPR	ES	Full system	Formation of unpaired electrons on O (holes versus superoxo-like species)	Directly captures and quantifies unpaired electron spins	Not all unpaired spins visible with standard methods (such as Mn^{3+}, Ni^{2+})	Understanding of EPR feature for peroxide needed	12
X-ray diffraction, PDF	OD	Bulk	Crystallographic O occupancy and position	Local structure refinements; O–O coordination environment; captures short covalent bonds	Disorder makes refinements challenging; difficult to determine the exact structural model	Well established for structural analysis	24,155,156
Neutron diffraction, PDF	Neutron diffraction: OD; PDF: ES	Bulk	Li-occupancy and O–O distances	Quantification of site occupancy of both Li and O; O–O local bonding environment	Large amount of material required; special cell design	In situ methodology for neutron PDF needed	49,102
Raman	OD	5–100 nm; SHINERS: <5 nm	Peroxide O–O vibrational modes (700–900 cm^{-1})	Captures $[O_2]^{n-}$ vibrational modes for reference (such as Li_2O_2)	SHINERS: surface sensitivity	In situ: benchmarking of highly ionic systems required	11,104,109, 110,112–114
NMR	ES	Full system	Li and M ordering	Sensitivity to chemical bonding environment and electronic structure	Careful computational modelling often needed to help correctly assign spectra; cannot easily probe paramagnetic metal centres	Benchmarking of ^{17}O NMR required	18,19,28, 48,116–119
Electron microscopy	OD	HRTEM and STEM: bulk and surface; EELS<100 nm	M migration, O dimers, dislocations, stacking faults	Atomic-resolution imaging; chemical environment sensitivity	Beam-induced artifacts; local information	Beam damage to highly charged sample must be mitigated	124–129

DEMS, differential electrochemical mass spectrometry; EELS, electron energy loss spectroscopy; EPR, electron paramagnetic resonance; ES, for the moment, ex situ only; EY, electron yield; FY, fluorescence yield; HAXPES, hard X-ray photoelectron spectroscopy; HRTEM, high-resolution transmission electron microscopy; OD, can be captured in operando; PDF, pair distribution function; RIXS, resonant inelastic X-ray scattering; SHINERS; shell-isolated nanoparticle-enhanced Raman spectroscopy; STEM, scanning transmission electron microscopy; STXM, scanning transmission X-ray microscopy; sXAS, soft X-ray absorption spectroscopy; XPS, X-ray photoelectron spectroscopy.

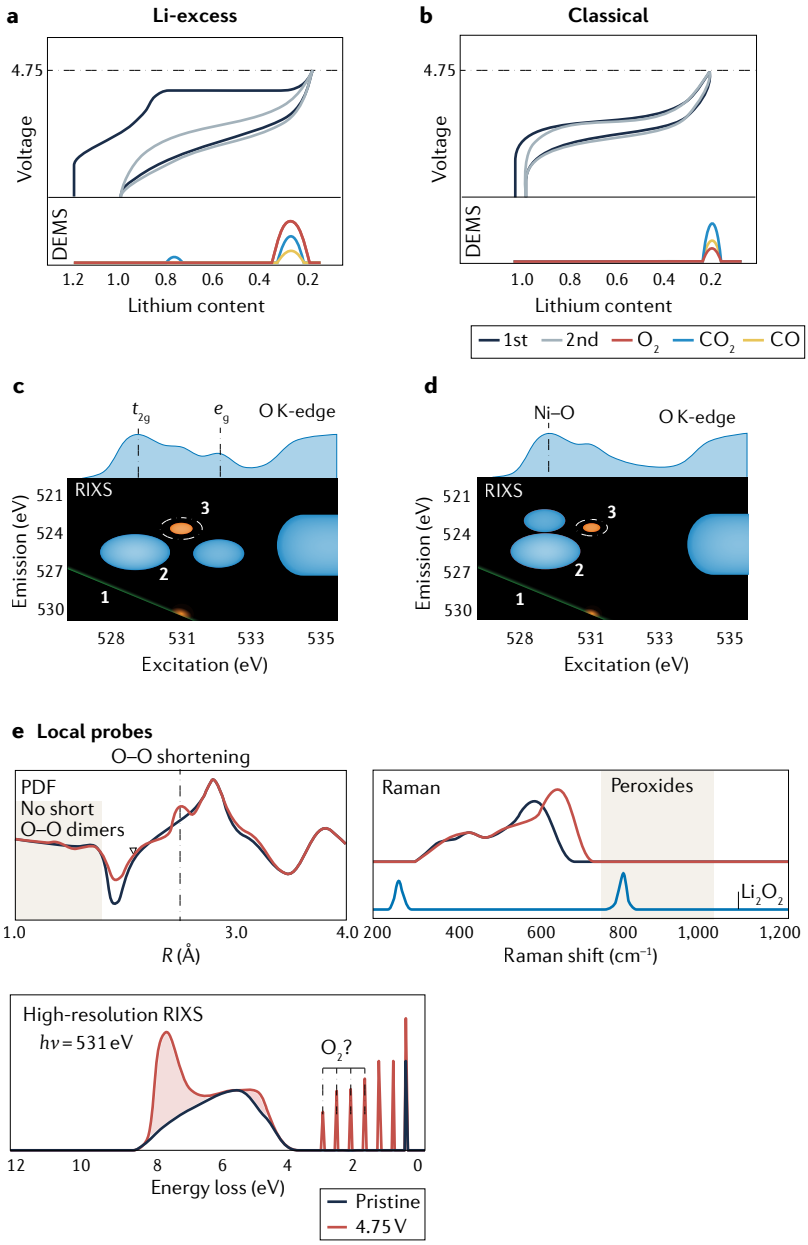

Fig. 6 | **Characterization tools for addressing capacity contributions and assigning the oxygen-redox mechanism. a,b** | Electrochemical profiles (top) of Li-excess (panel **a**) and classical layered oxides (panel **b**) along with the typical gas-release processes observed in operando differential electrochemical mass spectrometry (DEMS) (bottom), summarizing the key signatures reported[11,13,74,75,110]. **c,d** | Corresponding resonant inelastic X-ray scattering (RIXS) map representations (bottom) for Li-excess $Li_x(Ni_{1-y-z}Mn_yCo_z)O_2$ (NMC) (panel **c**) and $Li_x(Ni_{1-y-z}Co_yAl_z)O_2$ (NCA) (panel **d**) charged to 4.75 V, identifying the elastic peak (1), transition metal (M)–O hybridized features (2) and oxidized O feature (3) found in both types of system[23,65,69,81,82,84,92]. The representative soft X-ray absorption spectra shown above the RIXS maps can be obtained from the integrated intensity across the RIXS map at each excitation energy. **e** | Representative illustrations of neutron pair distribution function (PDF)[102,103,107] (where *R* is the O–O distance), Raman[11,109,110] and high-resolution RIXS spectra (where *hν* is the excitation energy) that have been used to assign O–O dimerization for Li-excess layered oxides[45,105]. Panel **a** adapted from REF.[11], Springer Nature Limited. Panel **b** adapted with permission from REF.[74], American Chemical Society. Panel **c** adapted from REF.[23], CC BY 4.0, and with permission from REF.[69], American Chemical Society. Panel **d** adapted with permission from REF.[65], RSC. Panel **e** (top) adapted with permission from REF.[102], Elsevier. Panel **e** (middle) adapted from REF.[11], Springer Nature Limited; from REF.[109], CC BY 4.0; and with permission from REF.[110], IOP © The Electrochemical Society. Reproduced by permission of IOP Publishing. All rights reserved. Panel **e** (bottom) adapted from REFS[45,105], Springer Nature Limited.

of the excess capacity arises from a novel, bulk redox mechanism.

Assignment of redox mechanism. Currently, the most widely used probes to directly assess oxygen redox are soft X-ray absorption spectroscopy (sXAS)[23,29] and resonant inelastic X-ray scattering (RIXS)[81,82]. This choice is largely due to the bulk sensitivity of these techniques with probing depths of >100 nm in fluorescence[66,81] and transmission[3,4] modes, enabling direct examination of the bulk oxygen environment. Indeed, spatially resolved scanning transmission X-ray microscopy (STXM) measurements of Li-excess NMC identified oxidized oxygen (O^{n-}) states that formed in the bulk but that were absent from the surface regions where transition metals were reduced[23]. Further details on sXAS[83] and RIXS[81,84] at the O K-edge can be found elsewhere. Looking more specifically at the bulk-sensitive O K-edge techniques, sXAS monitors excitations to the unoccupied O 2*p* states while RIXS also considers the subsequent emission decay processes from the excited state. The O K-edge RIXS maps include an elastic recombination emission line (green in FIG. 6c,d), fluorescent emission from density-of-state features associated with M–O hybridized states (blue in FIG. 6c,d) and Raman-like resonance excitations[85], such as phonons or charge-transfer processes (orange in FIG. 6c,d). The primary feature of interest in the RIXS map occurs at excitation and emission energies of 531 eV and 523.5 eV, respectively, which is an energetic range similar to that for known features of peroxides and O_2 gas[82,86]. In-depth RIXS measurements of Li-excess NMC revealed that the oxidized oxygen line shape consists of a second weak feature at 526.5 eV that is more spectroscopically consistent with observations for a range of peroxide systems than is the primary feature[69]. Whether this observation is evidence of a true peroxide remains up for debate (see below). In all studies, the 523.5-eV RIXS feature emerges after the end of conventional transition metal redox, correlates directly to the additional capacity and is reversibly lost on discharge as measured in ex situ experiments[23,80]. Moreover, this RIXS feature has been observed in both alkali-excess[23,87–90] and classical[65,91–93] layered oxides (FIG. 6c,d) despite the distinction often drawn between these two systems. However, the parent Li_2MnO_3 system displays no O^{n-} RIXS features, even when reaching high first-charge excess capacities (>350 mAh g^{-1})[51].

X-ray photoelectron spectroscopy (XPS) of the O 1*s* state has been considered a probe of peroxide-like states[94,95], particularly with the use of hard X-rays (namely, hard X-ray photoelectron spectroscopy (HAXPES)) for increased sub-surface sensitivity. Yet these techniques are still highly surface sensitive, limited to the top 5 nm, with recent work highlighting that the O 1*s* peroxide-like feature can arise from cathode surface degradation and electrolyte decomposition under conditions in which minimal oxygen redox is expected[96]. This clarification may account for discrepancies in previous publications that focus on Li-excess NMC, such as the claims of lower-voltage oxygen redox (4.1 V)[97] and irreversibility on discharge[95].

Beyond O K-edge spectroscopy, two other techniques that are less frequently used to investigate oxygen redox are acid titration combined with DEMS[74,80] and electron paramagnetic resonance (EPR). Following reaction pathways first established for Li_2O_2 in Li–air batteries[98], an acid-titration method (H_2SO_4 in H_2O) was developed to break down O^{n-} species to form O_2 gas that can be quantified in a DEMS setup. Applying this method to Li-excess NMC[80], the total amount of oxidized oxygen captured during acid titration closely matched what was expected beyond the conventional transition metal redox and was consistent with the O K-edge RIXS results. Although more work is needed to benchmark and confirm these assignments, the acid-titration technique in particular looks promising for chemically probing the nature of the oxidation products.

EPR provides chemical information about unpaired electron spins in a material, by measuring the deviation of the electron *g*-factors from the free-electron value (g_e) as a result of spin–orbit coupling (Supplementary Fig. 1). As applied to Li-excess materials, EPR has been used to infer the formation of 'peroxo-like' and 'superoxo-like' species in $Li_2Ru_{0.5}Sn_{0.5}O_3$ (REF.[12]). As peroxo species are not paramagnetic and therefore do not have EPR signals, the suffix 'like' was added by the authors to indicate an O–O bonded species associated with unpaired electron spin density. The emergence of a new EPR feature during the period in which the extra capacity is seen (Supplementary Fig. 1d) is an exciting result, particularly as this feature can be detected in situ[99]. However, in the in situ case, the *g* anisotropy is not resolved, which is expected for a superoxide species at low temperatures as indicated by simulations of CaO_2 (Supplementary Fig. 1c)[100]. Ultimately, more work is needed to determine the physical origin of this feature, because it is far from unambiguous.

Local structural motifs. Some of the principal questions in the anion-redox field are whether dimers are required for oxygen redox, the extent to which large (>2 Å)[82,101] or short (1.2–1.5 Å) dimers form, and whether dimers remain attached to the lattice. The primary structural assignments for O–O separation in anion-redox systems come from scattering techniques, neutron pair distribution function (PDF)[102,103], vibrational spectroscopy, Raman spectroscopy[11,87,104] and high-resolution RIXS[105] (FIG. 6e). Neutron PDF has revealed the shortening of interlayer O–O distances during the anionic-redox regime, with the shortest O–O separations in the range 2.3–2.5 Å for Li-excess NMC[102]. Similar O–O separations have been experimentally observed for materials with 4*d* ($Li_2Ru_{0.75}Sn_{0.25}O_3$)[106] and 5*d* ($Li_2IrO_3$)[107] metals and are often described as peroxo-like O–O dimerization. However, on the basis of computational analysis, it has been proposed that these small distortions of the O–O distance might be side effects of M–O hybridization within an extended π-bonded redox centre[15] rather than evidence of localized O–O interactions. Furthermore, these O–O separations are on par with, or longer, than those found in delithiated MO_2-type materials (NCA: ~2.5 Å (REF.[65]), $Na_{0.67}CoO_2$: ~2.30 Å (REF.[108])) (FIG. 6e, top left). The similarity of these scenarios raises the question of whether these O–O distortions are uniquely related to an oxygen-redox process or are a result of local structural distortions that occur during delithiation of the Li-excess material.

Much shorter O–O separations consistent with known molecular O_2 species have also been considered, particularly given the similarity of the RIXS features to these states[82,86] and the stabilization of molecular O_2^{n-} states in density functional theory calculations[27,42–44]. To date, ex situ Raman measurements have found no evidence of true peroxides forming in various 3*d* transition metal-based systems, including Li-excess NMC[11,109,110] and $Na_{2/3}[Mg_{0.28}Mn_{0.72}]O_2$ (REF.[87]) (FIG. 6e, top right). For a true peroxide, one might expect distortions that differ from those of the peroxo-like species that are associated with the transition metal environments. Given that other techniques that identify formation of oxidized oxygen are also performed ex situ (including acid titration[80] and O K-edge RIXS[81]), this result suggests that the reported RIXS feature does not correspond to peroxide states. Using a high-resolution spectrometer, two recent studies observed Raman-loss features for $Na_{0.75}[Li_{0.25}Mn_{0.75}]O_2$ (REF.[105]) and $Li_{1.2}Ni_{0.13}Co_{0.13}Mn_{0.54}O_2$ (REF.[45]) that are on-resonance with the O^{n-} states in RIXS and are indicative of an O–O separation of 1.2 Å (O_2 molecule). However, other studies have observed similar vibronic mode energies for both O_2 gas and an ill-defined peroxide within an amorphous Al_2O_3 structure, despite the 0.3-Å difference in O–O separation between these two systems[111]. Therefore, the vibrational spectra captured with RIXS might not provide an unambiguous assignment of the nature of the oxidized oxygen environment without additional modelling.

Operando Raman measurements have been thought to capture the formation of true peroxide states in alkali-excess systems[104,112–114], including Li-excess NMC[104]. However, these assignments have relied primarily on shell-isolated nanoparticle-enhanced Raman spectroscopy (SHINERS)[115], which is inherently surface sensitive (~1–5 nm)[104,112–115]. The top 5 nm of cathode particles are typically dominated by electrolyte degradation species[74] and reduced transition metal layers[23,74,96], raising the question of whether SHINERS probes the same type of oxidized oxygen states that are observed in bulk RIXS and acid titration. As with XPS and HAXPES[96], it will be important to benchmark this surface-sensitive method against high-voltage systems in which little to no oxygen redox is expected.

Another precise probe of local structure and short-range order is solid-state NMR. The observation and quantification of Li_2MnO_3-like ^6Li or ^7Li signals in $Li[Ni_xLi_{1/3-2x/3}Mn_{2/3-x/3}]O_2$ (REFS[18,19,48,116,117]) and Li-excess NMCs[28,118] has been crucial evidence in demonstrating that the excess Li in the transition metal layer is surrounded by six Mn^{4+} ions[117,119] rather than a stoichiometric mixture of transition metals. Beyond this local environment, the coherence length of Li_2MnO_3-like ordered domains is difficult to ascertain because this technique probes only the first cation coordination shell. Beyond the pristine state, NMR has been used to determine the order of sites from which Li ions are extracted during cycling. The Li ions in the Li layer are removed

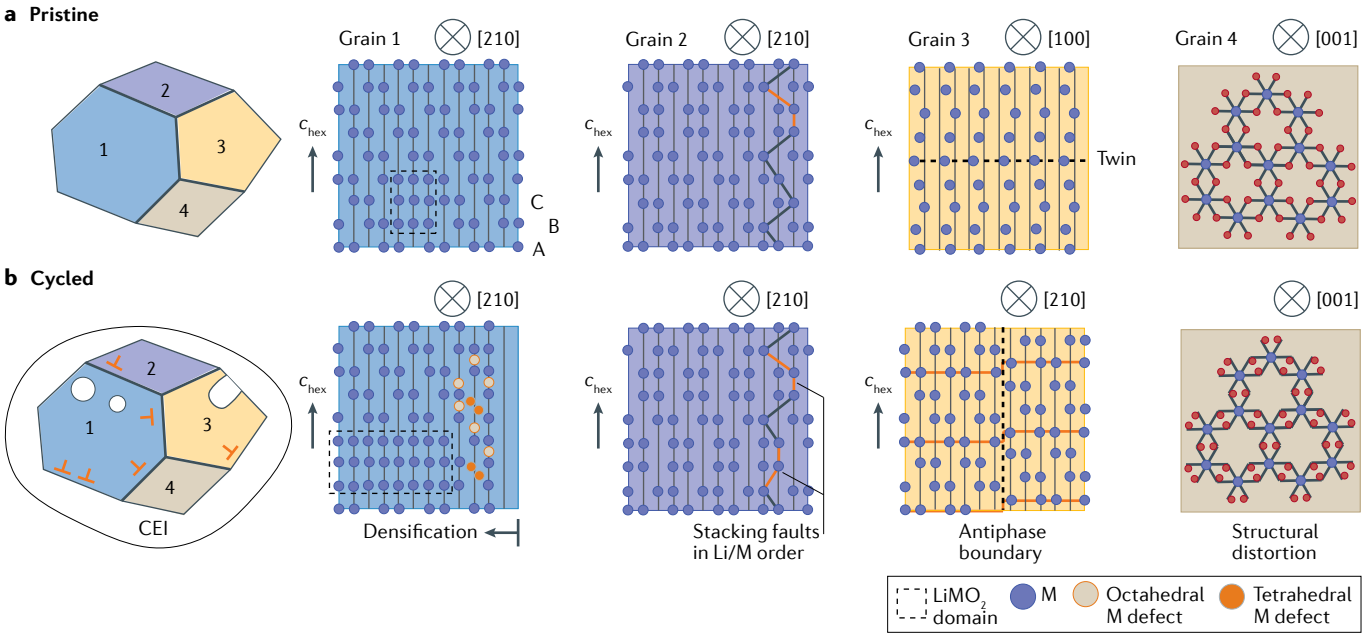

Fig. 7 | **Advanced analytical electron microscopy for studying anion-redox mechanisms in Li-excess layered oxides.** All the structures are based on the rhombohedral unit cell. The pristine material (panel **a**) contains a certain number of defects, including $LiMO_2$ domains (where M is a 3*d* transition metal), transition metal stacking faults and twin boundaries, as revealed by electron microscopy. The concentration of these defects increases after electrochemical activation (panel **b**). The formation of other types of defects has also been observed for the cycled material, including transition metal antisite defects, dislocations, antiphase grain boundaries and distortions of the oxygen lattice. In addition, oxygen vacancies form on the surface, accompanied by transition metal densification. A passivation layer — that is, cathode electrolyte interphase (CEI) — also forms through electrolyte decomposition. c_{hex} refers to the conventional *c* lattice vector of the hexagonal layered structure, oriented out of the plane of the cation layers.

at the beginning of charge[48], enabling the Li ions in the transition metal layer to drop into tetrahedral sites so that almost no octahedral Li remains in the transition metal layer at the onset of the 4.5-V activation process[47]. The remaining tetrahedral Li are removed during the 4.5-V process. The signal due to Li in the transition metal layer in $Li[Ni_xLi_{1/3-2x/3}Mn_{2/3-x/3}]O_2$ samples gradually disappears with cycle number; note that this signal can be removed in cases in which the samples have either been cycled to higher voltages or the electrochemistry has been optimized to extract more Li at 4.5–4.6 V (REFS[28,48]). On discharge, almost all anion-redox-active cathode materials yield broadened line shapes, reflecting an increase in the disorder of the transition metal ions. Using lower voltage cut-offs decreases the line-shape broadening, consistent with a decrease in bulk structural changes and the irreversibility typically associated with high-voltage processes. ^{17}O NMR has been used to probe oxygen ions directly, although most studies are limited to the pristine material. Stacking faults were identified in Li_2MnO_3 (REF.[120]), whereas in Li_2RuO_3, the presence of Ru–Ru dimers and the complex electronic structure were analysed[121]. Density functional theory studies have been used to help assign the NMR spectra. Although measurements on cycled materials are possible[122], the technical challenge of recording and analysing these spectra is amplified by the changing oxidation states and disordering that occurs. A recent study claimed to show the formation of O_2 molecules trapped in pockets within primary particles of Li-excess $Li_{1.2}Ni_{0.13}Co_{0.13}Mn_{0.54}O_2$ (REF.[45]). In this work, the authors referred to a previous study, in which the ^{17}O NMR spectrum of liquid O_2 was recorded[123], to support their assignment of the signals observed to molecular O_2, commenting that the width of the sideband manifold in their spectra is similar to the linewidth observed for liquid O_2. However, we note the similarity of the observed isotropic shifts in the charged material to those found for the oxygen environments in a closely related material, Li_2MnO_3, suggesting that further investigation is warranted before these signals can be definitively assigned to trapped O_2.

Finally, analytical scanning transmission electron microscopy (STEM) can provide real-space structural data with close-to-atomic resolution and has been widely used to document the structural signatures of anion redox. Annular dark-field (ADF) and annular bright-field (ABF) imaging combined with electron energy loss spectroscopy (EELS) provides sufficient contrast to distinguish M and O columns, and can provide electronic-structure information. These data have been used to demonstrate that pristine grains of Li-excess NMC consist of a coherent mixture of Li_2MnO_3-like honeycomb domains intergrown with $LiMO_2$ (REF.[124]) (FIG. 7), rather than a uniform solid solution of transition metal and Li ions. However, the structure is also not fully segregated into $xLi_2MnO_3 \bullet (1-x)LiMO_2$, given that the molar ratio between Li_2MnO_3 and $LiMO_2$ in local environments deviates from the initial stoichiometric design. Instead, each grain consists of a dominant Li_2MnO_3-like honeycomb ordering with $LiMO_2$ defect domains.

The out-of-plane structure contains a high concentration of transition metal stacking faults in the Li_2MnO_3-like crystalline regions. After charging through the activation plateau, EELS data suggests the formation of oxygen vacancies near the particle surface[125], which might facilitate migration of transition metal ions from the under-coordinated octahedral sites to the fully coordinated tetrahedral or octahedral sites in the Li layer[126]. In the Li_2IrO_3 model compound, ABF imaging revealed distortions of the O lattice (a decrease in the O–O distance to 2.5 Å), which has been interpreted as evidence of O–O dimerization[107] or delocalized π-redox[15]. The formation of other types of defects has also been identified, including dislocations[59], stacking faults[57], twin boundaries[126] and antiphase domains[127]. After extended cycling, the formation of large pores (~10 nm) was observed in the interior of the particle[128,129]. These observations derived from analytical electron microscopy indicate that the anion-redox reaction pathway probably involves multiple simultaneous processes guided by various new phases and defects. Given this complexity, exceptional care must be taken to exclude beam-induced artifacts in the characterization of cycled materials. Furthermore, insight from analytical electron microscopy provides limited statistical information and needs careful confirmation by other tools that provide global sample information.

Computational studies. An essential tool in the study of anion-redox processes is atomistic simulation based on electronic-structure methods. Given a structural model of a material, these techniques yield the bonding configuration and internal energy, which can be used to identify thermodynamically favourable configurations, compute electrochemical voltages and kinetic pathways, and inform thermochemical models[22,130]. These data are also used to generate spectroscopic[131], magnetic[132] and structural[133] characteristics of atomic environments to aid the interpretation of experimental observations. The computed electronic structure can be interpreted using molecular orbital theory through the analysis of bond lengths, magnetic moments and local projections of the computed wavefunction to assign oxidation states in the context of traditional electrochemical reactions. In particular, the signatures usually used to indicate anion oxidation are the presence of majority O states at the Fermi level, spin-polarization of O *p* orbitals and short O–O bond lengths (~1.6 Å for peroxides, ~1.3 Å for superoxides and ~1.2 Å for molecular O_2)[10,11,21,42,134]. It must, however, be noted that although these signatures of anion redox can routinely be found in high-energy states, the central challenge of a computational analysis lies in proving that any one of these states is either thermodynamically or kinetically favourable.

Computational techniques have been successful in producing precise models of cation redox, but the computational analysis of most anion-redox materials has been, at best, qualitative. A key observation from electronic-structure data is that O *p* orbitals that are not σ-bonded to a transition metal can form electrochemically active, high-energy states[10,11]. The effective hole concentration and computed voltage of these unbound O *p* states have been correlated with the accessibility of competing transition metal oxidation reactions[135], spectroscopic signatures[11,134] and various metrics of irreversibility and degradation[21]. However, studies based on broad structural enumeration and molecular dynamics have revealed that O *p* holes can be unstable with respect to a range of local relaxation processes involving transition metal migration or anion dimerization into O_2^{n-} species[14,42,44,105]. Resolving the nature of these local relaxations is a challenge, as the number of possible configurations is very large and the practical accessibility of any given pathway is strongly influenced by kinetics and microstructural features. Overcoming these obstacles is crucial for quantitative simulation of anion-redox processes and we call for renewed efforts to develop methods for efficient sampling and kinetic modelling.

A key requirement for simulating the structural evolution of anion-redox materials is that the chosen electronic-structure method must remain accurate for the diverse set of highly oxidized bonding environments that may arise. The most frequently used density functional theory methods — PBE + *U* (REFS[136,137]) and the hybrid HSE functional[138] — are calibrated using experimental and higher-order electronic-structure data taken from reduced materials[139,140]. An important detail overlooked in many studies is that these calibrations can break down in the presence of O–O bonding or highly oxidized transition metal environments: as one example, both PBE + *U* and HSE predict formation enthalpies of peroxides and permanganates that are much higher than experimental values (Supplementary Table 1), suggesting that these methods would not be able to account for the formation of these oxidation products. One solution is to use the recently introduced SCAN functional[141], which does not have a systematic error associated with O–O bonding[142]. However, SCAN is not a universal remedy because it is inherently less reliable in the representation of reduced transition metals, for which the PBE + *U* and HSE methods are known to work well[130]. Ultimately, it is imperative that any electronic-structure method used to study anion redox is calibrated to capture the specific reactions that might occur in highly oxidized environments.

Future perspectives

The development of practical high-performance cathodes that rely in part on anion redox requires both fundamental advances in understanding of the redox mechanisms that are responsible for the anomalous capacity of Li-excess materials and engineering strategies for controlling these processes to mitigate voltage hysteresis and decrease voltage decay. Given the multiscale behaviour of anion-redox materials, these efforts must span length scales from the electronic and atomic to the mesoscale and macroscale. Furthermore, as it is increasingly clear that anion redox is a highly metastable process, substantial progress is necessary towards understanding the role of kinetics in controlling the behaviour of these materials and how these kinetic processes can be altered through chemical and structural modifications.

The prerequisite to achieving these goals is the establishment of atomically precise structural models of both

the pristine state of the cathode and the material that forms after electrochemical activation. These data are essential to enable realistic computational studies of possible redox mechanisms. Owing to the prevalence of nanoscale inhomogeneities, as evidenced by electron microscopy[124], theoretical studies of averaged structures are unlikely to be fruitful, because the redox mechanisms responsible for the excess capacity may occur at interfaces between nanodomains or at extended structural defects. Furthermore, isolating favourable redox processes from detrimental decomposition reactions is not likely to be successful without first developing a detailed understanding of the crystal structure and its evolution.

The second goal is to resolve the ambiguities in the characterization of anion-redox processes by identifying reliable spectroscopic signatures to distinguish the possible oxidation products, notably the peroxide, superoxide and neutral O_2 molecular oxygen species. These data would facilitate quantification of the capacity arising from each redox process and its relationship to electrochemical performance metrics. At present, it is puzzling that while oxidized oxygen states appear similar to peroxide when using RIXS, there is no evidence of short (1.5 Å) O–O dimers in the bulk when using structural probes. The evidence for bulk neutral O_2 obtained from high-resolution RIXS is still under debate because the ^{17}O NMR assignment is not consistent with prior literature, and further benchmarking of materials and modelling are needed.

The third task is to establish the degree to which structural changes that accompany anion redox can be controlled, or whether they are an inseparable component of the electrochemical process. Although these structural transformations, which include transition metal migration and dislocation nucleation, correlate with irreversibility and hysteresis, they might also be a prerequisite for activating and facilitating the redox process. This apparent interplay between activating the redox process and structural defects calls for trade-offs in making use of anion redox: the more charge contribution from the oxygen ions, the more structural hysteresis might be induced during cycling.

Further work is needed to fully quantify the mechanism of anion redox, but substantial opportunities remain in mitigating voltage hysteresis and decreasing voltage decay by semi-empirically optimizing the composition of the cathode material. The poor electrochemical reversibility results from the fact that the charged state of a Li-excess cathode is a high-energy, metastable structure, the properties of which are controlled by an evolving structural disorder that appears during first-cycle activation. Capacity fade can be largely eliminated by protecting the particle surface through coating or reduced transition metal layers[13,143]. In an ideal scenario, voltage hysteresis and fade would be eliminated by minimizing bulk structural evolution, although it remains an open question whether anion redox is possible in the complete absence of structural change. The ideal structure of layered oxide Li-excess materials is able to accommodate a multitude of transition metals (such as Co, Ni and Mn) across a broad range of compositions. Variation in the transition metal composition and local order can greatly modify structural adaptability towards anion redox, both by changing the degree of hybridization with oxygen and by altering the activation energy of reaction pathways such as transition metal migration and O_2 gas evolution. Identifying compositions that maintain the pristine or activated structure and inhibit highly irreversible processes is thus an essential goal. Furthermore, given the role of microstructure in facilitating structural evolution and voltage hysteresis, it is necessary to identify compositions that yield mechanically robust structures that resist dislocation propagation, stacking fault formation and short-circuit transport of oxygen species. Finally, because the degradation of the metastable charged material becomes increasingly pronounced at high voltage, identifying compositions that decrease the charging voltage might be beneficial for preserving the structure of the charged state.

As an illustration of the considerable knowledge gap that exists today with respect to the role of transition metal composition on the electrochemical behaviour of Li-excess materials, we summarize several performance metrics for different Li-excess NM ($Li_{1+x}(Ni_{1-x-y}Mn_y)O_2$, $0<x<1$, $0<y<1$) and NMC ($Li_{1+x}(Ni_{1-x-y-z}Mn_yCo_z)O_2$, $0<x<1$, $0<y<1$, $0<z<1$) materials from the published literature in FIG. 8. Most of the published work focuses on a narrow range of transition metal ratios, leaving a broad space for further exploration. Nevertheless, among the compositions that have been reported in Li-excess NM and NMC materials, the initial charge capacity provided by non-conventional cation redox increases with Mn ion content. The initial Coulombic efficiency, correlated with the reversibility of anion redox, decreases with Mn content.

It is nonetheless clear that composition alone does not determine the performance of the cathode. For a given composition, capacity and Coulombic efficiency vary drastically between studies, which may stem from differences in synthesis method, particle morphology and phase purity of the pristine materials. The complexity of the testing setup makes literature comparisons even more challenging. To enable meaningful comparisons between different studies, it is crucial that all relevant battery testing parameters are reported, including the cell form factor and internal setup, electrode composition, active material loading, electrolyte composition and separator type. We suggest that the following battery testing practices should be used for Li-excess layered cathodes in order to be relevant for practical applications. First, the electrode should comprise at least 90% active materials by weight with careful porosity control. Second, the active mass loading should be >15 mg cm^{-2} (equivalent to 4 mAh cm^{-2} capacity loading). Third, the amount of electrolyte as well as the anode-to-cathode capacity ratio need to be well controlled, especially for assessing the effects of composition modifications on electrochemical performance. Finally, voltage hysteresis and fade should be quantified based on an appropriate electrochemical measurement.

The second notable opportunity in engineering Li-excess materials for long-term cycling stability is in improving the stability of the electrode–electrolyte interphase. Surface modification strategies have been

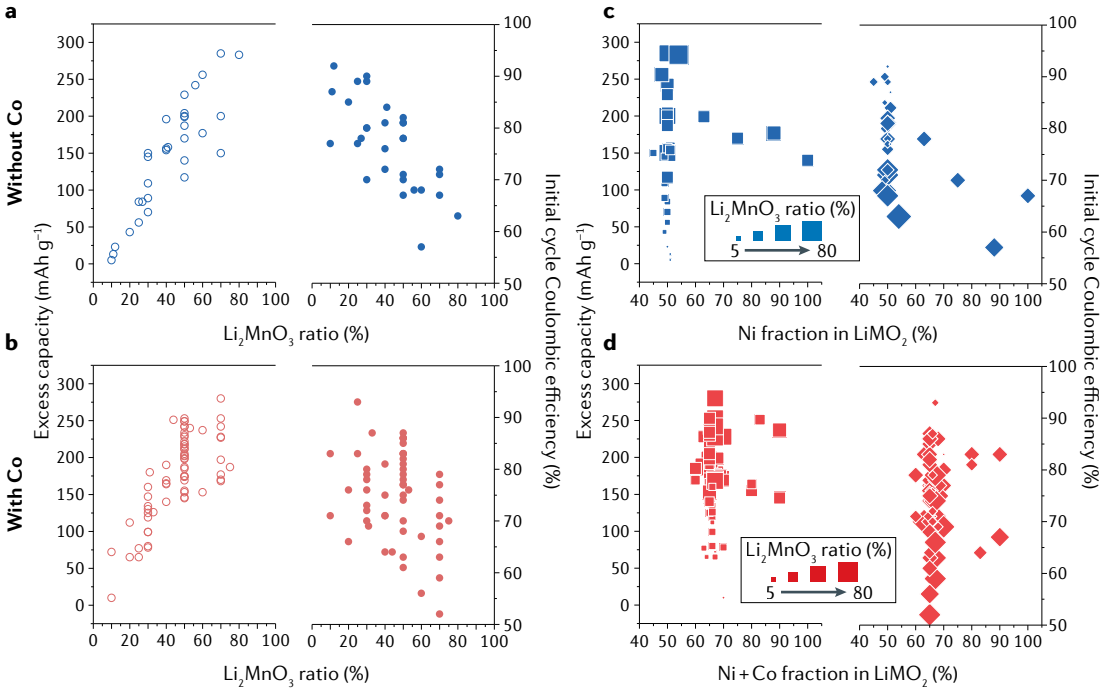

Fig. 8 | **Impact of sample composition on reversible and stable oxygen redox in Li-excess materials.** Excess capacity and initial cycle Coulombic efficiency for Li-excess $Li_{1+x}(Ni_{1-x-y}Mn_y)O_2$ (NM) (panel **a**) and $Li_{1+x}(Ni_{1-x-y-z}Mn_yCo_z)O_2$ (NMC) (panel **b**) as a function of Li_2MnO_3 ratio, and the excess capacity and initial cycle Coulombic efficiency for Li-excess NM (panel **c**) and NMC (panel **d**) as a function of transition metal (M) fraction in $LiMO_2$. Most studies have focused on a narrow range of transition metal ratios, and among the reported compositions in Li-excess NM and NMC materials, the amount of Mn has a direct impact on the excess charge capacity and Coulombic efficiency of the initial cycle. The molar ratio is calculated based on the composition formula $xLi_2MnO_3 \cdot (1-x)LiMO_2$ (REFS[50,157–196]). All data are for prepared samples with Mn^{4+} and Co^{3+} in the pristine state that have not been surface treated. All measurements were recorded in the half-cell setup, with Li metal as the counter electrode. The excess capacity equals the difference between initial charge capacity and capacity from conventional transition metal redox (that is, Ni^{2+} to Ni^{3+}, Ni^{3+} to Ni^{4+}, and Co^{3+} to Co^{4+}). For a fair comparison, all data are from half-cells tested with a similar voltage range and C-rate. Data are available in Supplementary Table 2.

widely applied to suppress O_2 gas evolution and mitigate capacity fade[13,144–146]. However, the compatibility of the electrolyte with the charged state is often neglected in the literature. The activation step that is ubiquitous in anion redox materials occurs at 4.5 V versus Li^+/Li^0. For the frequently used carbonate-based liquid electrolytes, the upper stable operating voltage is limited to 4.3–4.4 V. When the voltage is pushed above this limit (4.5 V), carbonate-based electrolytes decompose on the cathode surface and fail to form an effective passivating layer. The oxygen redox products, such as superoxide and peroxide species, or other radical anion complexes, readily react with this class of carbonate-based electrolyte. These parasitic side reactions not only destroy the lattice structure of cathode materials but also accelerate the consumption of the electrolyte, thereby leading to a rapid decay in electrochemical performance[147,148]. Different electrolyte systems need to be evaluated at high-voltage cutoffs, including additives based on fluorinated phosphate esters[149], all-fluorinated electrolytes[150], sulfone-based electrolytes[151] and localized high-concentration electrolytes[152].

In closing, we reflect on the steady progress of research into Li-excess layered materials over the past 25 years. Optimized Li-excess NMC materials can currently deliver reversible capacities close to 320 mAh g^{-1} with >90% Coulombic efficiency in the first cycle at room temperature. No obvious capacity decay is found after hundreds of cycles[153]. These results indicate that the excess capacity ascribed to anion redox can be reversibly maintained through a combination of composition tuning, surface protection, electrolyte choice and other engineering strategies. It is noteworthy that a specific energy of 450 Wh kg^{-1} at the cell level was demonstrated in 2020 for Li-excess materials using 5-Ah pouch cells[57]. Finally, while the voltage of Li-excess materials degrades over repeated cycling, the pristine structure and electrochemistry can be fully recovered through a moderate heating protocol[24]. This finding not only reveals the metastable state of cycled Li-excess layered materials, but also provides opportunities to discover anomalous emerging material properties, such as negative thermal expansion and negative compressibility[57,154].

The primary outstanding issues in anion-redox cathodes are voltage hysteresis and voltage fade, both of which are related to the structural evolution of the cathode material. Several reports have pointed to promising design strategies that may be able to address these problems. For example, a change of the stacking order of the pristine material from the common O3 type to an O2 structure[29] might help to suppress irreversible metal migration, whereas a change in the long-range ordering

of Li in the transition metal layer away from the common honeycomb structure might eliminate voltage hysteresis[105]. In both cases, the key to improved electrochemical performance is structural control. Although the mechanistic origin of anion redox remains uncertain, the accessibility of structural transformations distinguishes all reactions that have been proposed in the literature: structure-preserving oxidation based on oxygen-hole formation or π-redox, and structure-altering oxidation based on transition metal migration or molecular oxygen formation. By controlling the kinetics of structural transformations, it is thus possible that materials will be driven from one anion-redox mechanism to another, possibly decreasing hysteresis and voltage fade in the process. For example, despite the issue of electrolyte incompatibility, non-hysteretic anion redox has been achieved in layered Na–Mn–O materials (for example, $Na_2Mn_3O_7$ and $Na_{0.6}Li_{0.2}Mn_{0.8}O_2$) for at least several tens of cycles because both Li and Mn ions are kinetically immobile in the structure and, thus, inhibit the irreversible transformation[15,20,103,105]. Ultimately, further progress depends on a fundamental understanding of the thermodynamics and kinetics of anion redox. Resolving these basic electrochemical questions requires a synergy of spectroscopic, imaging and computational techniques and will enable both the rational optimization of Li-excess cathodes and broad applications to other functional, metastable material systems.

Published online: 08 February 2022

1. Liu, J. et al. Pathways for practical high-energy long-cycling lithium metal batteries. *Nat. Energy* **4**, 180–186 (2019).
2. Radin, M. D. et al. Narrowing the gap between theoretical and practical capacities in Li-ion layered oxide cathode materials. *Adv. Energy Mater.* **7**, 1602888 (2017).
3. Amatucci, G. G., Tarascon, J. M. & Klein, C. CoO_2, the end member of the $LiCoO_2$ solid solution. *J. Electrochem. Soc.* **143**, 1114–1123 (1996).
4. Liu, H. et al. Identifying the chemical and structural irreversibility in $LiNi_{0.8}Co_{0.15}Al_{0.05}O_2$ — a model compound for classical layered intercalation. *J. Mater. Chem. A* **6**, 4189–4198 (2018).
5. Lu, Z., MacNeil, D. D. & Dahn, J. R. Layered cathode materials $Li[Ni_xLi_{(1/3-2x/3)}Mn_{[2/3-x/3]}]O_2$ for lithium-ion batteries. *Electrochem. Solid-State Lett.* **4**, A191 (2001).
6. Hy, S. et al. Performance and design considerations for lithium excess layered oxide positive electrode materials for lithium ion batteries. *Energy Environ. Sci.* **9**, 1931–1954 (2016).
7. Grimaud, A., Hong, W. T., Shao-Horn, Y. & Tarascon, J. M. Anionic redox processes for electrochemical devices. *Nat. Mater.* **15**, 121–126 (2016).
8. Okubo, M. & Yamada, A. Molecular orbital principles of oxygen-redox battery electrodes. *ACS Appl. Mater. Interfaces* **9**, 36463–36472 (2017).
9. Li, B. & Xia, D. Anionic redox in rechargeable lithium batteries. *Adv. Mater.* **29**, 1701054 (2017).
10. Seo, D.-H. et al. The structural and chemical origin of the oxygen redox activity in layered and cation-disordered Li-excess cathode materials. *Nat. Chem.* **8**, 692–697 (2016).
11. Luo, K. et al. Charge-compensation in 3*d*-transition-metal-oxide intercalation cathodes through the generation of localized electron holes on oxygen. *Nat. Chem.* **8**, 684–691 (2016).
12. Sathiya, M. et al. Reversible anionic redox chemistry in high-capacity layered-oxide electrodes. *Nat. Mater.* **12**, 827–835 (2013).
13. Qiu, B. et al. Gas–solid interfacial modification of oxygen activity in layered oxide cathodes for lithium-ion batteries. *Nat. Commun.* **7**, 12108 (2016).
14. Radin, M. D., Vinckeviciute, J., Seshadri, R. & Van der Ven, A. Manganese oxidation as the origin of the anomalous capacity of Mn-containing Li-excess cathode materials. *Nat. Energy* **4**, 639–646 (2019).
15. Kitchaev, D. A., Vinckeviciute, J. & Van der Ven, A. Delocalized metal–oxygen π-redox is the origin of anomalous nonhysteretic capacity in Li-Ion and Na-ion cathode materials. *J. Am. Chem. Soc.* **143**, 1908–1916 (2021).
16. Delmas, C., Fouassier, C. & Hagenmuller, P. Structural classification and properties of the layered oxides. *Physica B+C* **99**, 81–85 (1980).
17. Thackeray, M. M. et al. Li_2MnO_3-stabilized $LiMO_2$ (M = Mn, Ni, Co) electrodes for lithium-ion batteries. *J. Mater. Chem.* **17**, 3112–3125 (2007).
18. Yoon, W. S. et al. Local structure and cation ordering in O3 lithium nickel manganese oxides with stoichiometry $Li[Ni_xMn_{(2-x)/3}Li_{(1-2x)/3}]O_2$ NMR studies and first principles calculations. *Electrochem. Solid-State Lett.* **7**, A167–A171 (2004).
19. Bréger, J. et al. High-resolution X-ray diffraction, DIFFaX, NMR and first principles study of disorder in the Li_2MnO_3 $Li[Ni_{1/2}Mn_{1/2}]O_2$ solid solution. *J. Solid State Chem.* **178**, 2575–2585 (2005).
20. Mortemard de Boisse, B. et al. Highly reversible oxygen-redox chemistry at 4.1 V in $Na_{x/7-x}[\square_{1/7}Mn_{6/7}]O_2$ (□: Mn vacancy). *Adv. Energy Mater.* **8**, 1800409 (2018).
21. Ben Yahia, M., Vergnet, J., Saubanère, M. & Doublet, M. L. Unified picture of anionic redox in Li/Na-ion batteries. *Nat. Mater.* **18**, 496–502 (2019).
22. Van Der Ven, A., Deng, Z., Banerjee, S. & Ong, S. P. Rechargeable alkali-ion battery materials: theory and computation. *Chem. Rev.* **120**, 6977–7019 (2020).
23. Gent, W. E. et al. Coupling between oxygen redox and cation migration explains unusual electrochemistry in lithium-rich layered oxides. *Nat. Commun.* **8**, 2091 (2017).
24. Li, Y. et al. Regeneration of degraded Li-rich layered oxide materials through heat treatment-induced transition metal reordering. *Energy Storage Mater.* **35**, 99–107 (2021).
25. Croy, J. R., Balasubramanian, M., Gallagher, K. G. & Burrell, A. K. Review of the U.S. Department of Energy's 'deep dive' effort to understand voltage fade in Li- and Mn-rich cathodes. *Acc. Chem. Res.* **48**, 2813–2821 (2015).
26. Sathiya, M. et al. Origin of voltage decay in high-capacity layered oxide electrodes. *Nat. Mater.* **14**, 230–238 (2015).
27. Vinckeviciute, J., Kitchaev, D. A. & Van Der Ven, A. A two-step oxidation mechanism controlled by Mn migration explains the first-cycle activation behavior of Li_2MnO_3-based Li-excess materials. *Chem. Mater.* **33**, 1625–1636 (2021).
28. Dogan, F. et al. Re-entrant lithium local environments and defect driven electrochemistry of Li- and Mn-rich Li-ion battery cathodes. *J. Am. Chem. Soc.* **137**, 2328–2335 (2015).
29. Eum, D. et al. Voltage decay and redox asymmetry mitigation by reversible cation migration in lithium-rich layered oxide electrodes. *Nat. Mater.* **19**, 419–427 (2020).
30. Aydinol, M., Kohan, A., Ceder, G., Cho, K. & Joannopoulos, J. Ab initio study of lithium intercalation in metal oxides and metal dichalcogenides. *Phys. Rev. B* **56**, 1354–1365 (1997).
31. Wolverton, C. & Zunger, A. First-principles prediction of vacancy order-disorder and intercalation battery voltages in Li_xCoO_2. *Phys. Rev. Lett.* **81**, 606–609 (1998).
32. Van der Ven, A., Aydinol, M., Ceder, G., Kresse, G. & Hafner, J. First-principles investigation of phase stability. *Phys. Rev. B* **58**, 2975–2987 (1998).
33. Graetz, J. et al. Electronic structure of chemically-delithiated $LiCoO_2$ studied by electron energy-loss spectrometry. *J. Phys. Chem. B* **106**, 1286–1289 (2002).
34. Roychoudhury, S. et al. Deciphering the oxygen absorption pre-edge: a caveat on its application for probing oxygen redox reactions in batteries. *Energy Environ. Mater.* **4**, 246–254 (2020).
35. Bo, S. H., Li, X., Toumar, A. J. & Ceder, G. Layered-to-rock-salt transformation in desodiated Na_xCrO_2(x 0.4). *Chem. Mater.* **28**, 1419–1429 (2016).
36. Kubota, K. et al. New insight into structural evolution in layered $NaCrO_2$ during electrochemical sodium extraction. *J. Phys. Chem. C* **119**, 166–175 (2015).
37. Jones, C. D. W., Rossen, E. & Dahn, J. R. Structure and electrochemistry of $Li_xCr_yCo_{1-y}O_2$. *Solid State Ion.* **68**, 65–69 (1994).
38. Lyu, Y. et al. Atomic insight into electrochemical inactivity of lithium chromate ($LiCrO_2$): irreversible migration of chromium into lithium layers in surface regions. *J. Power Sources* **273**, 1218–1225 (2015).
39. Pan, C., Lee, Y. J., Ammundsen, B. & Grey, C. P. ^{6}Li MAS NMR studies of the local structure and electrochemical properties of Cr-doped lithium manganese and lithium cobalt oxide cathode materials for lithium-ion batteries. *Chem. Mater.* **14**, 2289–2299 (2002).
40. Croy, J. R., Garcia, J. C., Iddir, H., Trask, S. E. & Balasubramanian, M. Harbinger of hysteresis in lithium-rich oxides: anionic activity or defect chemistry of cation migration. *J. Power Sources* **471**, 228335 (2020).
41. Xie, Y., Saubanère, M. & Doublet, M.-L. Requirements for reversible extra-capacity in Li-rich layered oxides for Li-ion batteries. *Energy Environ. Sci.* **10**, 266–274 (2017).
42. Hong, J. et al. Metal–oxygen decoordination stabilizes anion redox in Li-rich oxides. *Nat. Mater.* **18**, 256–265 (2019).
43. Marusczyk, A. et al. Oxygen activity and peroxide formation as charge compensation mechanisms in Li_2MnO_3. *J. Mater. Chem. A* **5**, 15183–15190 (2017).
44. Chen, H. & Islam, M. S. Lithium extraction mechanism in Li-rich Li_2MnO_3 involving oxygen hole formation and dimerization. *Chem. Mater.* **28**, 6656–6663 (2016).
45. House, R. A. et al. First-cycle voltage hysteresis in Li-rich 3*d* cathodes associated with molecular O_2 trapped in the bulk. *Nat. Energy* **5**, 777–785 (2020).
46. Oishi, M. et al. Direct observation of reversible oxygen anion redox reaction in Li-rich manganese oxide, Li_2MnO_3, studied by soft X-ray absorption spectroscopy. *J. Mater. Chem. A* **4**, 9293–9302 (2016).
47. Jiang, M., Key, B., Meng, Y. S. & Grey, C. P. Electrochemical and structural study of the layered, 'Li-excess' lithium-ion battery electrode material $Li[Li_{1/9}Ni_{1/5}Mn_{5/9}]O_2$. *Chem. Mater.* **21**, 2733–2745 (2009).
48. Grey, C. P., Yoon, W. S., Reed, J. & Ceder, G. Electrochemical activity of Li in the transition-metal sites of O3 $Li[Li_{(1-2x)}/3Mn_{(2-x)}/3Ni_x]O_2$. *Electrochem. Solid-State Lett.* **7**, A290 (2004).
49. Liu, H. et al. Operando lithium dynamics in the Li-rich layered oxide cathode material via neutron diffraction. *Adv. Energy Mater.* **6**, 1502143 (2016).
50. Lu, Z. & Dahn, J. R. Understanding the anomalous capacity of $Li/Li[Ni_xLi_{(1/3-2x/3)}Mn_{(2/3-x/3)}]O_2$ cells using in situ X-ray diffraction and electrochemical studies. *J. Electrochem. Soc.* **149**, A815 (2002).
51. Rana, J. et al. Quantifying the capacity contributions during activation of Li_2MnO_3. *ACS Energy Lett.* **5**, 634–641 (2020).

52. Qiao, Y., Jiang, K., Deng, H. & Zhou, H. A high-energy-density and long-life lithium-ion battery via reversible oxide–peroxide conversion. *Nat. Catal.* **2**, 1035–1044 (2019).
53. Zhu, Z. et al. Anion-redox nanolithia cathodes for Li-ion batteries. *Nat. Energy* **1**, 16111 (2016).
54. Qiao, Y., Deng, H., He, P. & Zhou, H. A 500 Wh/kg Lithium-metal cell based on anionic redox. *Joule* **4**, 1445–1458 (2020).
55. Xu, B., Fell, C. R., Chi, M. & Meng, Y. S. Identifying surface structural changes in layered Li-excess nickel manganese oxides in high voltage lithium ion batteries: a joint experimental and theoretical study. *Energy Environ. Sci.* **4**, 2223–2233 (2011).
56. Singer, A. et al. Nucleation of dislocations and their dynamics in layered oxide cathode materials during battery charging. *Nat. Energy* **3**, 641–647 (2018).
57. Qiu, B. et al. Metastability and reversibility of anionic redox-based cathode for high-energy rechargeable batteries. *Cell Rep. Phys. Sci.* **1**, 100028 (2020).
58. Yu, H. et al. Electrochemical kinetics of the $0.5Li_2MnO_3 \cdot 0.5LiMn_{0.42}Ni_{0.42}Co_{0.16}O_2$ 'composite' layered cathode material for lithium-ion batteries. *RSC Adv.* **2**, 8797–8807 (2012).
59. Li, Q. et al. Dynamic imaging of crystalline defects in lithium-manganese oxide electrodes during electrochemical activation to high voltage. *Nat. Commun.* **10**, 1692 (2019).
60. Klinser, G. et al. Continuous monitoring of the bulk oxidation states in $Li_xNi_{1/3}Mn_{1/3}Co_{1/3}O_2$ during charging and discharging. *Appl. Phys. Lett.* **109**, 213901 (2016).
61. Klinser, G. et al. Charging of lithium cobalt oxide battery cathodes studied by means of magnetometry. *Solid. State Ion.* **293**, 64–71 (2016).
62. Balasubramanian, M., Sun, X., Yang, X. Q. & Mcbreen, J. In situ X-ray absorption studies of a high-rate $LiNi_{0.85}Co_{0.15}O_2$ cathode material. *J. Electrochem. Soc.* **147**, 2903–2909 (2000).
63. Petersburg, C. F., Li, Z., Chernova, N. A., Whittingham, M. S. & Alamgir, F. M. Oxygen and transition metal involvement in the charge compensation mechanism of $LiNi_{1/3}Mn_{1/3}Co_{1/3}O_2$ cathodes. *J. Mater. Chem.* **22**, 19993–20000 (2012).
64. Li, W., Asl, H. Y., Xie, Q. & Manthiram, A. Collapse of $LiNi_{1-x-y}Co_xMn_yO_2$ lattice at deep charge irrespective of nickel content in lithium-ion batteries. *J. Am. Chem. Soc.* **141**, 5097–5101 (2019).
65. Lebens-Higgins, Z. W. et al. Revisiting the charge compensation mechanisms in $LiNi_{0.8}Co_{0.2-y}Al_yO_2$ systems. *Mater. Horiz.* **6**, 2112–2123 (2019).
66. Liu, X. et al. Why $LiFePO_4$ is a safe battery electrode: Coulomb repulsion induced electron-state reshuffling upon lithiation. *Phys. Chem. Chem. Phys.* **17**, 26369–26377 (2015).
67. Qiao, R. et al. Transition-metal redox evolution in $LiNi_{0.5}Mn_{0.3}Co_{0.2}O_2$ electrodes at high potentials. *J. Power Sources* **360**, 294–300 (2017).
68. Zhuo, Z. et al. Effect of excess lithium in $LiMn_2O_4$ and $Li_{1.15}Mn_{1.85}O_4$ electrodes revealed by quantitative analysis of soft X-ray absorption spectroscopy. *Appl. Phys. Lett.* **110**, 093902 (2017).
69. Lebens-Higgins, Z. W. et al. Distinction between intrinsic and X-ray-induced oxidized oxygen states in Li-rich 3*d* layered oxides and $LiAlO_2$. *J. Phys. Chem. C* **123**, 13201–13207 (2019).
70. Koga, H. et al. Operando X-ray absorption study of the redox processes involved upon cycling of the Li-rich layered oxide $Li_{1.20}Mn_{0.54}Co_{0.13}Ni_{0.13}O_2$ in Li ion batteries. *J. Phys. Chem. C* **118**, 5700–5709 (2014).
71. Ito, A. et al. In situ X-ray absorption spectroscopic study of Li-rich layered cathode material $Li[Ni_{0.17}Li_{0.2}Co_{0.07}Mn_{0.56}]O_2$. *J. Power Sources* **196**, 6828–6834 (2011).
72. Oishi, M. et al. Charge compensation mechanisms in $Li_{1.16}Ni_{0.15}Co_{0.19}Mn_{0.50}O_2$ positive electrode material for Li-ion batteries analyzed by a combination of hard and soft X-ray absorption near edge structure. *J. Power Sources* **222**, 45–51 (2013).
73. Renfrew, S. E. & McCloskey, B. D. Residual lithium carbonate predominantly accounts for first cycle CO_2 and CO outgassing of Li-stoichiometric and Li-rich layered transition-metal oxides. *J. Am. Chem. Soc.* **139**, 17853–17860 (2017).
74. Renfrew, S. E. & McCloskey, B. D. Quantification of surface oxygen depletion and solid carbonate evolution on the first cycle of $LiNi_{0.6}Mn_{0.2}Co_{0.2}O_2$ electrodes. *ACS Appl. Energy Mater.* **2**, 3762–3772 (2019).
75. Rinkel, B. L. D., Hall, D. S., Temprano, I. & Grey, C. P. Electrolyte oxidation pathways in lithium-ion batteries. *J. Am. Chem. Soc.* **142**, 15058–15074 (2020).
76. Hatsukade, T., Schiele, A., Hartmann, P., Brezesinski, T. & Janek, J. Origin of carbon dioxide evolved during cycling of nickel-rich layered NCM cathodes. *ACS Appl. Mater. Interfaces* **10**, 38892–38899 (2018).
77. Wandt, J., Freiberg, A. T. S., Ogrodnik, A. & Gasteiger, H. A. Singlet oxygen evolution from layered transition metal oxide cathode materials and its implications for lithium-ion batteries. *Mater. Today* **21**, 825–833 (2018).
78. Guerrini, N. et al. Charging mechanism of Li_2MnO_3. *Chem. Mater.* **32**, 3733–3740 (2020).
79. Massel, F. et al. Excess lithium in transition metal layers of epitaxially grown thin film cathodes of Li_2MnO_3 leads to rapid loss of covalency during first battery cycle. *J. Phys. Chem. C* **123**, 28519–28526 (2019).
80. Ramakrishnan, S., Park, B., Wu, J., Yang, W. & McCloskey, B. D. Extended interfacial stability through simple acid rinsing in a Li-rich oxide cathode material. *J. Am. Chem. Soc.* **142**, 8522–8531 (2020).
81. Yang, W. & Devereaux, T. P. Anionic and cationic redox and interfaces in batteries: advances from soft X-ray absorption spectroscopy to resonant inelastic scattering. *J. Power Sources* **389**, 188–197 (2018).
82. Gent, W. E., Abate, I. I., Yang, W., Nazar, L. F. & Chueh, W. C. Design rules for high-valent redox in intercalation electrodes. *Joule* **4**, 1369–1397 (2020).
83. Frati, F., Hunault, M. O. J. Y. & De Groot, F. M. F. Oxygen K-edge X-ray absorption spectra. *Chem. Rev.* **120**, 4056–4110 (2020).
84. Wu, J., Yang, Y. & Yang, W. Advances in soft X-ray RIXS for studying redox reaction states in batteries. *Dalt. Trans.* **49**, 13519–13527 (2020).
85. Kotani, A. & Shin, S. Resonant inelastic X-ray scattering spectra for electrons in solids. *Rev. Mod. Phys.* **73**, 203–246 (2001).
86. Zhuo, Z. et al. Full energy range resonant inelastic X-ray scattering of O_2 and CO_2: direct comparison with oxygen redox state in batteries. *J. Phys. Chem. Lett.* **11**, 2618–2623 (2020).
87. Maitra, U. et al. Oxygen redox chemistry without excess alkali-metal ions in $Na_{2/3}[Mg_{0.28}Mn_{0.72}]O_2$. *Nat. Chem.* **10**, 288–295 (2018).
88. Dai, K. et al. High reversibility of lattice oxygen redox quantified by direct bulk probes of both anionic and cationic redox reactions. *Joule* **3**, 518–541 (2019).
89. Wu, J. et al. Dissociate lattice oxygen redox reactions from capacity and voltage drops of battery electrodes. *Sci. Adv.* **6**, eaaw3871 (2020).
90. House, R. A. et al. Lithium manganese oxyfluoride as a new cathode material exhibiting oxygen redox. *Energy Environ. Sci.* **11**, 926–932 (2018).
91. Zhang, J. N. et al. Trace doping of multiple elements enables stable battery cycling of $LiCoO_2$ at 4.6 V. *Nat. Energy* **4**, 594–603 (2019).
92. Li, N. et al. Unraveling the cationic and anionic redox reactions in a conventional layered oxide cathode. *ACS Energy Lett.* **4**, 2836–2842 (2019).
93. Lee, A. G., Wu, J., Kim, D. & Cho, K. Reversible anionic redox activities in conventional $LiNi_{1/3}Co_{1/3}Mn_{1/3}O_2$ cathodes. *Angew. Chem. Int. Ed.* **59**, 8681–8688 (2020).
94. Assat, G. et al. Fundamental interplay between anionic/cationic redox governing the kinetics and thermodynamics of lithium-rich cathodes. *Nat. Commun.* **8**, 2219 (2017).
95. Uchimoto, Y. et al. Oxidation behaviour of lattice oxygen in Li-rich manganese-based layered oxide studied by hard X-ray photoelectron spectroscopy. *J. Mater. Chem. A* **4**, 5909–5916 (2016).
96. Lebens-higgins, Z. W. et al. How bulk sensitive is hard X-ray photoelectron spectroscopy: accounting for the cathode–electrolyte interface when addressing oxygen redox. *J. Phys. Chem. Lett.* **11**, 2106–2112 (2020).
97. Naylor, A. J. et al. Depth-dependent oxygen redox activity in lithium-rich layered oxide cathodes. *J. Mater. Chem. A* **7**, 25355–25368 (2019).
98. Mccloskey, B. D. et al. Combining accurate O_2 and Li_2O_2 assays to separate discharge and charge stability limitations in nonaqueous Li-O_2 batteries. *J. Phys. Chem. Lett.* **4**, 2989–2993 (2013).
99. Sathiya, M. et al. Electron paramagnetic resonance imaging for real-time monitoring of Li-ion batteries. *Nat. Commun.* **6**, 6276 (2015).
100. Che, M. & Tench, A. J. in *Advances in Catalysis* Vol. 32 (eds Eley, D. D., Pines, H. & Weisz, P. B.) 1–148 (Elsevier, 1983).
101. Assat, G. & Tarascon, J. M. Fundamental understanding and practical challenges of anionic redox activity in Li-ion batteries. *Nat. Energy* **3**, 373–386 (2018).
102. Zhao, E. et al. Local structure adaptability through multi cations for oxygen redox accommodation in Li-rich layered oxides. *Energy Storage Mater.* **24**, 384–393 (2020).
103. Rong, X. et al. Structure-induced reversible anionic redox activity in Na layered oxide cathode. *Joule* **2**, 125–140 (2018).
104. Li, X. et al. Direct visualization of the reversible O^{2-}/O^- redox process in Li-rich cathode materials. *Adv. Mater.* **30**, 1705197 (2018).
105. House, R. A. et al. Superstructure control of first-cycle voltage hysteresis in oxygen-redox cathodes. *Nature* **577**, 502–508 (2020).
106. Assat, G., Iadecola, A., Delacourt, C., Dedryvère, R. & Tarascon, J.-M. Decoupling cationic–anionic redox processes in a model Li-rich cathode via operando X-ray absorption spectroscopy. *Chem. Mater.* **29**, 9714–9724 (2017).
107. McCalla, E. et al. Visualization of O–O peroxo-like dimers in high-capacity layered oxides for Li-ion batteries. *Science* **350**, 1516–1521 (2015).
108. Wang, H. et al. Short O–O separation in layered oxide $Na_{0.67}CoO_2$ enables an ultrafast oxygen evolution reaction. *Proc. Natl Acad. Sci. USA* **116**, 23473–23479 (2019).
109. Luo, K. et al. Anion redox chemistry in the cobalt free 3*d* transition metal oxide intercalation electrode $Li[Li_{0.2}Ni_{0.2}Mn_{0.6}]O_2$. *J. Am. Chem. Soc.* **138**, 11211–11218 (2016).
110. Ruther, R. E., Callender, A. F., Zhou, H., Martha, S. K. & Nanda, J. Raman microscopy of lithium-manganese-rich transition metal oxide cathodes. *J. Electrochem. Soc.* **162**, A98–A102 (2014).
111. Arhammar, C. et al. Unveiling the complex electronic structure of amorphous metal oxides. *Proc. Natl Acad. Sci. USA* **108**, 6355–6360 (2011).
112. Li, Q. et al. Both cationic and anionic co-(de) intercalation into a metal-oxide material. *Joule* **2**, 1134–1145 (2018).
113. Zhang, X. et al. Manganese-based Na-rich materials boost anionic redox in high-performance layered cathodes for sodium-ion batteries. *Adv. Mater.* **31**, 1807770 (2019).
114. Cao, X. et al. Stabilizing reversible oxygen redox chemistry in layered oxides for sodium-ion batteries. *Adv. Energy Mater.* **10**, 1903785 (2020).
115. Li, J. F. et al. Shell-isolated nanoparticle-enhanced Raman spectroscopy. *Nature* **464**, 392–395 (2010).
116. Breger, J., Kang, K., Cabana, J., Ceder, G. & Grey, C. P. NMR, PDF and RMC study of the positive electrode material $Li(Ni_{0.5}Mn_{0.5})O_2$ synthesized by ion-exchange methods. *J. Mater. Chem.* **17**, 3167 (2007).
117. Buzlukov, A. L. et al. Li-rich Mn/Ni layered oxide as electrode material for lithium batteries: a ^{7}Li MAS NMR study revealing segregation into (nanoscale) domains with highly different electrochemical behaviors. *J. Phys. Chem. C* **120**, 19049–19063 (2016).
118. Iddir, H. et al. Pristine-state structure of lithium-ion-battery cathode material $Li_{1.2}Mn_{0.4}Co_{0.4}O_2$ derived from NMR bond pathway analysis. *J. Mater. Chem. A* **3**, 11471–11477 (2015).
119. Bréger, J. et al. Short- and long-range order in the positive electrode material, $Li(NiMn)_{0.5}O_2$: a joint X-ray and neutron diffraction, pair distribution function analysis and NMR study. *J. Am. Chem. Soc.* **127**, 7529–7537 (2005).
120. Seymour, I. D. et al. Characterizing oxygen local environments in paramagnetic battery materials via ^{17}O NMR and DFT calculations. *J. Am. Chem. Soc.* **138**, 9405–9408 (2016).
121. Reeves, P. J., Seymour, I. D., Griffith, K. J. & Grey, C. P. Characterizing the structure and phase transition of Li_2RuO_3 using variable-temperature ^{17}O and ^{7}Li NMR spectroscopy. *Chem. Mater.* **31**, 2814–2821 (2019).
122. Geng, F. et al. Monitoring the evolution of local oxygen environments during $LiCoO_2$ charging via ex situ ^{17}O NMR. *Chem. Commun.* **55**, 7550–7553 (2019).

123. Dundon, J. M. ^{17}O NMR in liquid O_2. *J. Chem. Phys.* **76**, 2171–2173 (1982).
124. Yu, H. et al. Crystalline grain interior configuration affects lithium migration kinetics in Li-rich layered oxide. *Nano Lett.* **16**, 2907–2915 (2016).
125. Carroll, K. J. et al. Probing the electrode/electrolyte interface in the lithium excess layered oxide $Li_{1.2}Ni_{0.2}Mn_{0.6}O_2$. *Phys. Chem. Chem. Phys.* **15**, 11128–11138 (2013).
126. Yin, W. et al. Structural evolution at the oxidative and reductive limits in the first electrochemical cycle of $Li_{1.2}Ni_{0.13}Mn_{0.54}Co_{0.13}O_2$. *Nat. Commun.* **11**, 1252 (2020).
127. Lyu, Y. et al. Correlations between transition-metal chemistry, local structure, and global structure in $Li_2Ru_{0.5}Mn_{0.5}O_3$ investigated in a wide voltage window. *Chem. Mater.* **29**, 9053–9065 (2017).
128. Hu, E. et al. Evolution of redox couples in Li- and Mn-rich cathode materials and mitigation of voltage fade by reducing oxygen release. *Nat. Energy* **3**, 690–698 (2018).
129. Yan, P. et al. Injection of oxygen vacancies in the bulk lattice of layered cathodes. *Nat. Nanotechnol.* **14**, 602–608 (2019).
130. Urban, A., Seo, D.-H. & Ceder, G. Computational understanding of Li-ion batteries. *npj Comput. Mater.* **2**, 16002 (2016).
131. Zheng, C. et al. Automated generation and ensemble-learned matching of X-ray absorption spectra. *npj Comput. Mater.* **4**, 12 (2018).
132. Clément, R. J., Kitchaev, D., Lee, J. & Ceder, G. Short-range order and unusual modes of nickel redox in a fluorine-substituted disordered rocksalt oxide lithium-ion cathode. *Chem. Mater.* **30**, 6945–6956 (2018).
133. Ji, H. et al. Hidden structural and chemical order controls lithium transport in cation-disordered oxides for rechargeable batteries. *Nat. Commun.* **10**, 592 (2019).
134. Yabuuchi, N. et al. Origin of stabilization and destabilization in solid-state redox reaction of oxide ions for lithium-ion batteries. *Nat. Commun.* **7**, 13814 (2016).
135. Lee, J. et al. Reversible Mn^{2+}/Mn^{4+} double redox in lithium-excess cathode materials. *Nature* **556**, 185–190 (2018).
136. Perdew, J. P., Burke, K. & Ernzerhof, M. Generalized gradient approximation made simple. *Phys. Rev. Lett.* **77**, 3865–3868 (1996).
137. Dudarev, S. & Botton, G. Electron-energy-loss spectra and the structural stability of nickel oxide: an LSDA+U study. *Phys. Rev. B* **57**, 1505–1509 (1998).
138. Heyd, J., Scuseria, G. E. & Ernzerhof, M. Hybrid functionals based on a screened Coulomb potential. *J. Chem. Phys.* **118**, 8207 (2003).
139. Seo, D. H., Urban, A. & Ceder, G. Calibrating transition-metal energy levels and oxygen bands in first-principles calculations: accurate prediction of redox potentials and charge transfer in lithium transition-metal oxides. *Phys. Rev. B* **92**, 115118 (2015).
140. Jain, A. et al. Formation enthalpies by mixing GGA and GGA + U calculations. *Phys. Rev. B* **84**, 045115 (2011).
141. Sun, J., Ruzsinszky, A. & Perdew, J. P. Strongly constrained and appropriately normed semilocal density functional. *Phys. Rev. Lett.* **115**, 036402 (2015).
142. Zhang, Y. et al. Efficient first-principles prediction of solid stability: towards chemical accuracy. *npj Comput. Mater.* **4**, 9 (2018).
143. Liu, H. et al. Understanding the role of NH_4F and Al_2O_3 surface co-modification on lithium-excess layered oxide $Li_{1.2}Ni_{0.2}Mn_{0.6}O_2$. *ACS Appl. Mater. Interfaces* **7**, 19189–19200 (2015).
144. Oh, P., Ko, M., Myeong, S., Kim, Y. & Cho, J. A novel surface treatment method and new insight into discharge voltage deterioration for high-performance $0.4Li_2MnO_3$-$0.6LiNi_{1/3}Co_{1/3}Mn_{1/3}O_2$ cathode materials. *Adv. Energy Mater.* **4**, 1400631 (2014).
145. Zheng, F. et al. Nanoscale surface modification of lithium-rich layered-oxide composite cathodes for suppressing voltage fade. *Angew. Chem. Int. Ed.* **54**, 13058–13062 (2015).
146. Zhu, Z. et al. Gradient Li-rich oxide cathode particles immunized against oxygen release by a molten salt treatment. *Nat. Energy* **4**, 1049–1058 (2019).
147. Xu, K. Nonaqueous liquid electrolytes for lithium-based rechargeable batteries. *Chem. Rev.* **104**, 4303–4417 (2004).
148. Xu, K. Electrolytes and interphases in Li-ion batteries and beyond. *Chem. Rev.* **114**, 11503–11618 (2014).
149. von Cresce, A. & Xu, K. Electrolyte additive in support of 5 V Li ion chemistry. *J. Electrochem. Soc.* **158**, A337 (2011).
150. Fan, X. et al. Non-flammable electrolyte enables Li-metal batteries with aggressive cathode chemistries. *Nat. Nanotechnol.* **13**, 715–722 (2018).
151. Alvarado, J. et al. A carbonate-free, sulfone-based electrolyte for high-voltage Li-ion batteries. *Mater. Today* **21**, 341–353 (2018).
152. Chen, S. et al. High-voltage lithium-metal batteries enabled by localized high-concentration electrolytes. *Adv. Mater.* **30**, 1706102 (2018).
153. Song, B. et al. A facile cathode design combining Ni-rich layered oxides with Li-rich layered oxides for lithium-ion batteries. *J. Power Sources* **325**, 620–629 (2016).
154. Zhang, M. et al. High pressure effect on structural and electrochemical properties of anionic redox-based lithium transition metal oxides. *Matter* **4**, 164–181 (2021).
155. Li, J., Shunmugasundaram, R., Doig, R. & Dahn, J. R. In situ X-ray diffraction study of layered Li-Ni-Mn-Co oxides: effect of particle size and structural stability of core-shell materials. *Chem. Mater.* **28**, 162–171 (2016).
156. Kleiner, K. et al. Origin of high capacity and poor cycling stability of Li-rich layered oxides: a long-duration in situ synchrotron powder diffraction study. *Chem. Mater.* **30**, 3656–3667 (2018).
157. Croy, J. R., Gallagher, K. G., Balasubramanian, M., Long, B. R. & Thackeray, M. M. Quantifying hysteresis and voltage fade in xLi_2MnO_3•$(1-x)LiMn_{0.5}Ni_{0.5}O_2$ electrodes as a function of Li_2MnO_3 content. *J. Electrochem. Soc.* **161**, 318–325 (2014).
158. Zhang, L., Borong, W., Ning, L. & Feng, W. Hierarchically porous micro-rod lithium-rich cathode material $Li_{1.2}Ni_{0.13}Mn_{0.54}Co_{0.13}O_2$ for high performance lithium-ion batteries. *Electrochim. Acta* **118**, 67–74 (2014).
159. Jin, X., Xu, Q., Yuan, X., Zhou, L. & Xia, Y. Synthesis, characterization and electrochemical performance of $Li[Li_{0.2}Mn_{0.54}Ni_{0.13}Co_{0.13}]O_2$ cathode materials for lithium-ion batteries. *Electrochim. Acta* **114**, 605–610 (2013).
160. Kim, D., Croy, J. R. & Thackeray, M. M. Comments on stabilizing layered manganese oxide electrodes for Li batteries. *Electrochem. Commun.* **36**, 103–106 (2013).
161. He, W. et al. Coprecipitation-gel synthesis and degradation mechanism of octahedral $Li_{1.2}Mn_{0.54}Ni_{0.13}Co_{0.13}O_2$ as high-performance cathode materials for lithium-ion batteries. *ACS Appl. Mater. Interfaces* **10**, 23018–23028 (2018).
162. Zheng, F. et al. The effect of composite organic acid (citric acid & tartaric acid) on microstructure and electrochemical properties of $Li_{1.2}Mn_{0.54}Ni_{0.13}Co_{0.13}O_2$ Li-rich layered oxides. *J. Power Sources* **346**, 31–39 (2017).
163. Wang, M.-J., Yu, F.-D., Sun, G., Gu, D.-M. & Wang, Z.-B. Optimizing the structural evolution of Li-rich oxide cathode materials via microwave-assisted pre-activation. *ACS Appl. Energy Mater.* **1**, 4158–4168 (2018).
164. Tang, Z., Wang, Z., Li, X. & Peng, W. Preparation and electrochemical properties of Co-doped and none-doped $Li[Li_xMn_{0.65(1-x)}Ni_{0.35(1-x)}]O_2$ cathode materials for lithium battery batteries. *J. Power Sources* **204**, 187–192 (2012).
165. Tang, Z., Wang, Z., Li, X. & Peng, W. Influence of lithium content on the electrochemical performance of $Li_{1+x}(Mn_{0.533}Ni_{0.233}Co_{0.233})_{1-x}O_2$ cathode materials. *J. Power Sources* **208**, 237–241 (2012).
166. Martha, S. K., Nanda, J., Veith, G. M. & Dudney, N. J. Electrochemical and rate performance study of high-voltage lithium-rich composition: $Li_{1.2}Mn_{0.525}Ni_{0.175}Co_{0.1}O_2$. *J. Power Sources* **199**, 220–226 (2012).
167. Oishi, M. et al. Direct observation of reversible charge compensation by oxygen ion in Li-rich manganese layered oxide positive electrode material, $Li_{1.16}Ni_{0.15}Co_{0.19}Mn_{0.50}O_2$. *J. Power Sources* **276**, 89–94 (2015).
168. Li, B., Yu, Y. & Zhao, J. Facile synthesis of spherical $xLi_2MnO_3 \cdot (1-x)Li(Mn_{0.33}Co_{0.33}Ni_{0.33})O_2$ as cathode materials for lithium-ion batteries with improved electrochemical performance. *J. Power Sources* **275**, 64–72 (2015).
169. Johnson, C. S., Li, N., Lefief, C., Vaughey, J. T. & Thackeray, M. M. Synthesis, characterization and electrochemistry of lithium battery electrodes: $xLi_2MnO_3 \cdot (1-x)LiMn_{0.333}Ni_{0.333}Co_{0.333}O_2$ ($0 \le x \le 0.7$). *Chem. Mater.* **20**, 6095–6106 (2008).
170. Kang, S.-H. & Thackeray, M. M. Stabilization of xLi_2MnO_3·$(1-x)LiMO_2$ electrode surfaces (M=Mn, Ni, Co) with mildly acidic, fluorinated solutions. *J. Electrochem. Soc.* **155**, A269 (2008).
171. Croy, J. R. et al. Countering the voltage decay in high capacity $xLi_2MnO_3 \cdot (1-x)LiMO_2$ electrodes (M=Mn, Ni, Co) for Li^+-ion batteries. *J. Electrochem. Soc.* **159**, 781–790 (2012).
172. Liu, J., Liu, J., Wang, R. & Xia, Y. Degradation and structural evolution of $xLi_2MnO_3 \cdot (1-x)LiMn_{1/3}Ni_{1/3}Co_{1/3}O_2$ during cycling. *J. Electrochem. Soc.* **161**, A160–A167 (2014).
173. R.N., R., Bosubabu, D., Karthick, K. B. & Ramesha, K. Tuning of Ni, Mn, and Co (NMC) content in $0.4(LiNi_xMn_yCo_zO_2) \cdot 0.4(Li_2MnO_3)$ toward stable high-capacity lithium-rich cathode materials. *ACS Appl. Energy Mater.* **3**, 10872–10881 (2020).
174. Shen, S. et al. Tuning electrochemical properties of Li-rich layered oxide cathodes by adjusting Co/Ni ratios and mechanism investigation using in situ X-ray diffraction and online continuous flow differential electrochemical mass spectrometry. *ACS Appl. Mater. Interfaces* **10**, 12666–12677 (2018).
175. Sun, G. et al. Local electronic structure modulation enhances operating voltage in Li-rich cathodes. *Nano Energy* **66**, 104102 (2019).
176. Konishi, H., Gunji, A., Feng, X. & Furutsuki, S. Effect of transition metal composition on electrochemical performance of nickel-manganese-based lithium-rich layer-structured cathode materials in lithium-ion batteries. *J. Solid State Chem.* **249**, 80–86 (2017).
177. Verde, M. G. et al. Effect of morphology and manganese valence on the voltage fade and capacity retention of $Li[Li_{2/12}Ni_{3/12}Mn_{7/12}]O_2$. *ACS Appl. Mater. Interfaces* **6**, 18868–18877 (2014).
178. Liu, H. et al. Communication-enhancing the electrochemical performance of lithium-excess layered oxide $Li_{1.13}Ni_{0.3}Mn_{0.57}O_2$ via a facile nanoscale surface modification. *J. Electrochem. Soc.* **163**, 971–973 (2016).
179. Lengyel, M. et al. Composition optimization of layered lithium nickel manganese cobalt oxide materials synthesized via ultrasonic spray pyrolysis. *J. Electrochem. Soc.* **161**, A1338–A1349 (2014).
180. Fell, C. R., Carroll, K. & Meng, Y. S. Synthesis-structure-property relations in layered 'Li-Excess' oxides electrode materials $Li[Li_{1/3-2x/3}Ni_xMn_{2/3-x/3}]O_2$ (x = 1/3, 1/4 and 1/5). *J. Electrochem. Soc.* **157**, A1202 (2010).
181. Zhang, M., Liu, H., Liu, Z., Fang, C. & Meng, Y. S. Modified coprecipitation synthesis of mesostructure-controlled Li-rich layered oxides for minimizing voltage degradation. *ACS Appl. Energy Mater.* **1**, 3369–3376 (2018).
182. Kim, D. et al. Composite 'layered-layered-spinel' cathode structures for lithium-ion batteries. *J. Electrochem. Soc.* **160**, A31–A38 (2013).
183. Liu, J. et al. General synthesis of $xLi_2MnO_3 \cdot (1-x)LiMn_{1/3}Ni_{1/3}Co_{1/3}O_2$ nanomaterials by a molten-salt method: towards a high capacity and high power cathode for rechargeable lithium batteries. *J. Mater. Chem.* **22**, 25380–25387 (2012).
184. Amalraj, F. et al. Synthesis of integrated cathode materials xLi_2MnO_3·$(1-x)LiMn_{1/3}Ni_{1/3}Co_{1/3}O_2$ (x=0.3, 0.5, 0.7) and studies of their electrochemical behavior. *J. Electrochem. Soc.* **157**, A1121 (2010).
185. Li, X. et al. Preparation and electrochemical performances of $xLi_2MnO_3(1-x)LiNi_{0.45}Co_{0.2}Mn_{0.35}O_2$ ($0 \le x \le 1$) for high-power lithium-ion batteries. *Ceram. Int.* **44**, 17062–17068 (2018).
186. Yuan, T., Liu, H. Q., Gu, Y. J., Cui, H. Z. & Wang, Y. M. The phase structure and electrochemical performance of $xLi_2MnO_3 \cdot (1-x)LiNi_{1/3}Co_{1/3}Mn_{1/3}O_2$ during the synthesis and charge–discharge process. *Appl. Phys. A* **122**, 812 (2016).
187. Riekehr, L. et al. Effect of pristine nanostructure on first cycle electrochemical characteristics of lithium-rich lithium-nickel-cobalt-manganese-oxide cathode ceramics for lithium ion batteries. *J. Power Sources* **306**, 135–147 (2016).
188. Li, J., Li, M., Zhang, L. & Wang, J. General synthesis of: $xLi_2MnO_3 \cdot (1-x)LiNi_{1/3}Co_{1/3}Mn_{1/3}O_2$ (x = 1/4, 1/3, and 1/2) hollow microspheres towards enhancing the performance of rechargeable lithium ion batteries. *J. Mater. Chem. A* **4**, 12442–12450 (2016).

189. Ates, M. N., Mukerjee, S. & Abraham, K. M. A search for the optimum lithium rich layered metal oxide cathode material for Li-ion batteries. *J. Electrochem. Soc.* **162**, A1236–A1245 (2015).
190. Li, J., Xu, Y., Li, X. & Zhang, Z. Li_2MnO_3 stabilized $LiNi_{1/3}Co_{1/3}Mn_{1/3}O_2$ cathode with improved performance for lithium ion batteries. *Appl. Surf. Sci.* **285**, 235–240 (2013).
191. Ma, D., Zhang, P., Li, Y. & Ren, X. $Li_{1.2}Mn_{0.54}Ni_{0.13}Co_{0.13}O_2$-encapsulated carbon nanofiber network cathodes with improved stability and rate capability for Li-ion batteries. *Sci. Rep.* **5**, 11257 (2015).
192. Peralta, D. et al. Role of the composition of lithium-rich layered oxide materials on the voltage decay. *J. Power Sources* **280**, 687–694 (2015).
193. Noh, J. K. et al. Mechanochemical synthesis of Li_2MnO_3 shell/$LiMO_2$ (M = Ni, Co, Mn) core-structured nanocomposites for lithium-ion batteries. *Sci. Rep.* **4**, 4847 (2014).
194. Ghanty, C., Basu, R. N. & Majumder, S. B. Performance of wet chemical synthesized xLi_2MnO_3-$(1-x)Li(Mn_{0.375}Ni_{0.375}Co_{0.25})O_2$ $(0.0 \leq x \leq 1.0)$ integrated cathode for lithium rechargeable battery. *J. Electrochem. Soc.* **159**, 1125–1134 (2012).
195. Pimenta, V. et al. Synthesis of Li-rich NMC: a comprehensive study. *Chem. Mater.* **29**, 9923–9936 (2017).
196. Dai, D. et al. Li-rich layered $Li_{1.2}Mn_{0.54}Ni_{0.13}Co_{0.13}O_2$ derived from transition metal carbonate with a micro-nanostructure as a cathode material for high-performance Li-ion batteries. *RSC Adv.* **6**, 96714–96720 (2016).

Acknowledgements
The authors acknowledge funding support from the NorthEast Center for Chemical Energy Storage (NECCES), an Energy Frontier Research Center funded by the US Department of Energy, Office of Science, Office of Basic Energy Sciences under Award No. DE-SC0012583. The authors thank J.-M. Doux, W. Li, H. Chung and B. Sayahpour for their help in preparing the electrochemical performance summary (Supplementary Table 2) from published papers.

Author contributions
All authors contributed to the discussion of content, writing and editing of the manuscript prior to submission.

Competing Interests
The authors declare no competing interests.

Peer review information
Nature Reviews Materials thanks Khalil Amine, Laurent Duda and the other, anonymous, reviewer(s) for their contribution to the peer review of this work.

Publisher's note
Springer Nature remains neutral with regard to jurisdictional claims in published maps and institutional affiliations.

Supplementary information
The online version contains supplementary material available at https://doi.org/10.1038/s41578-022-00416-1.

© Springer Nature Limited 2022